JGR Space Physics

RESEARCH ARTICLE
10.1029/2022JA031175

Global Dynamical Network of the Spatially Correlated Pc2 Wave Response for the 2015 St. Patrick's Day Storm

S. Chaudhry[1], S. C. Chapman[1,2], J. Gjerloev[3,4], and C. D. Beggan[5]

[1]Department of Physics, Centre for Fusion, Space and Astrophysics, University of Warwick, Coventry, UK, [2]Department of Mathematics and Statistics, University of Tromso, Tromso, Norway, [3]The Johns Hopkins University Applied Physics Laboratory, Laurel, MD, USA, [4]Department of Physics and Technology, University of Bergen, Bergen, Norway, [5]British Geological Survey, Edinburgh, UK

Key Points:

- First global network analysis of Pc2 wave activity using 100+ magnetometers at 1 s cadence
- Novel method to construct the dynamical network of globally coherent Pc2 wave activity
- Network parameters reveal the global magnetospheric response in the 2015 St. Patrick's Day storm

Correspondence to:

S. Chaudhry,
shahbaz.chaudhry@warwick.ac.uk

Citation:

Chaudhry, S., Chapman, S. C., Gjerloev, J., & Beggan, C. D. (2023). Global dynamical network of the spatially correlated Pc2 wave response for the 2015 St. Patrick's Day storm. *Journal of Geophysical Research: Space Physics*, *128*, e2022JA031175. https://doi.org/10.1029/2022JA031175

Received 21 NOV 2022
Accepted 18 APR 2023

Abstract We show the global dynamics of spatial correlation of Pc2 wave activity can track the evolution of the 2015 St. Patrick's Day geomagnetic storm for an 8 hr time window around onset. The global spatially coherent response is tracked by forming a dynamical network from 1 s data using the full set of 100+ ground-based magnetometer stations collated by SuperMAG and Intermagnet. The pattern of spatial coherence is captured by network parameters which in turn track the evolution of the storm. At onset interplanetary magnetic field (IMF) $B_z > 0$ and Pc2 power increases, we find a global response with stations correlated over both local and global distances. Following onset, whilst $B_z > 0$, the network response is confined to the day-side. When IMF $B_z < 0$, there is a strong local response at high latitudes, consistent with the onset of polar cap convection driven by day-side reconnection. The spatially coherent response as revealed by the network grows and is maximal when auroral (SuperMAG electrojet) and ring current (SuperMAG ring current) 1 min resolution geomagnetic indices peak, consistent with an active electrojet and ring-current. Throughout the storm there is a coherent response both in stations located along lines of constant geomagnetic longitude, between hemispheres, and across magnetic local time. The network does not simply track average Pc2 wave power, it is characterized by network parameters which track the storm evolution. This is the first study to parameterize global Pc2 wave correlation and offers the possibility of statistical studies across multiple events and comparison with, and validation of, space weather models.

Plain Language Summary Space weather poses a risk to infrastructure including satellites and power systems. A key challenge within space weather is predicting the magnetospheric response. To better understand geomagnetic activity, we (for the first time) build a dynamical network to parameterize the Pc2 wave response. Closed magnetic field lines in the inner magnetosphere can support standing Alfven waves (a magnetic "harp") and these are measured on the ground as Pc waves which occupy distinct frequency bands. Pc waves are excited by a variety of processes related to space weather. Previous work has focused on chains of magnetometers that are at constant magnetic longitude which sample the different resonant frequencies of the "harp" (different field line lengths). Recently, SuperMAG has begun to offer second resolution data which allows higher frequency Pc2 waves to be resolved and studied globally. Our first results are a study of an intense isolated geomagnetic storm where we have identified network parameters and have shown that these track the distinct phases of the storm in terms of spatial coherence of Pc2 wave activity. Using these network parameters we can perform statistical studies across many storms and quantitatively benchmark space weather models with observations.

1. Introduction

Reconfiguration of solar coronal field-lines can lead to an energetic release of plasma known as a coronal mass ejection (CME) (Schwenn, 2006). If the CME is incident on the magnetosphere with interplanetary magnetic field (IMF) $B_z < -10$ nT and duration $t > 3$ hr, an extreme space weather event known as a geomagnetic storm is induced (Gonzalez et al., 1994; Pulkkinen, 2007). In order to understand the dynamics of geomagnetic storms, we can study ultralow frequency (ULF) waves which are field line resonances (FLR) along closed field lines in the inner magnetosphere (Baumjohann & Treumann, 2012; Hughes, 1994; McPherron et al., 1972; Southwood & Hughes, 1983). During a storm there are a number of driving forces, both internal (magnetospheric) and external (solar wind), that can give rise to ULF waves. External ULF wave drivers include shear flow between the magnetosphere and the solar wind (McPherron et al., 1972; Yumoto, 1988) and the rapid displacement of field

lines during storm sudden commencement (SSC). When measured using ground-based magnetometers, ULF waves are classified as Pc waves and occupy distinct frequency bands (Jacobs et al., 1964). The Pc2/Pi2 band has been studied extensively both in terms of basic physics and also as an indicator of processes that take place in the magnetosphere/ionosphere during geomagnetic storms (Arnoldy et al., 1996; Chisham & Orr, 1997; Katsavrias et al., 2021; Liu et al., 2012; Rasinkangas et al., 1994). Generation mechanisms for Pc2 waves (which we focus on in this paper) include ion-cyclotron resonance at equatorial regions of the magnetosphere (Kozyra et al., 1997; Murphy et al., 2014). Hence, Pc2 waves are effective at depleting relativistic electrons from the outer radiation belts and ring current, leading to redistribution of plasma along field lines through pitch angle scattering and thus modulating the duration of geomagnetic storms (Engebretson et al., 2008; Kitamura et al., 1988; Kozyra et al., 1997; Menk, 2011).

In this paper, we study Pc2 wave excitation as a globally coherent phenomenon. We analyze an 8 hr time window around onset for the well known St. Patrick's Day event on the 17th of March 2015 (Wu et al., 2016). Previous work has detailed the ionospheric effect of the storm (Mahrous et al., 2018; Maurya et al., 2018), electron precipitation from the radiation belts (Clilverd et al., 2020) and observations of global navigation satellite system (GNSS) disturbances (Jacobsen & Andalsvik, 2016). To analyze the global spatial correlation of Pc2 wave activity we create networks. First used in discrete mathematics, networks have become a useful tool in dynamical systems and have been used extensively in fields such as ecology, control systems, and particle physics (Newman, 2018; Strogatz, 2001). The dynamic networks we refer to in this paper are often known as functional networks in neuroscience and adaptive networks in statistical physics (Castillo, 1998; Kozma & Barrat, 2008). Dynamical network structure and evolution can be used to parameterize the system and underlying processes (Boccaletti et al., 2006). In geophysics, networks have been used to characterize ionospheric total electron content (McGranaghan et al., 2017), ground induced current in response to storms (Orr, Chapman, & Beggan, 2021) and substorm ionospheric current systems (Orr, Chapman, Gjerloev, et al., 2021). In other fields of geophysics, namely seismology, networks can be created from earthquake data (Abe & Suzuki, 2006; Pastén et al., 2018).

The time dependent network will be built from observations using the full set of 100+ globally distributed ground-based magnetometer stations, curated by the SuperMAG/Intermagnet collaborations. Networks have been previously used successfully with 1 min resolution SuperMAG data to obtain the timings of the high latitude response to IMF B_z turnings (Dods et al., 2017) and the evolution of high latitude current systems during substorms (Dods et al., 2015; Orr et al., 2019, 2021a). For the first time we perform network analysis with 1 s high resolution data that resolve Pc2 waves. Our analysis demonstrates that Pc2 wave cross-correlation between globally spatially distributed observations can track the evolution of the storm in terms of evolving physical processes. The Pc2 wave band is optimal because the frequency is low enough to be well resolved by 1 s measurements, and high enough to have a relatively short cross-correlation time window. Therefore, we build dynamical Pc2 networks to chart the time evolution of full spatio-temporal pattern of coherence under active conditions.

To build Pc dynamical networks, we first band-pass filter ground magnetometer data and then use the filtered waveforms, that is, the narrow banded oscillatory signal to build a time-varying matrix of cross-correlation between all pairs of ground stations. Thresholding this matrix provides a set of network connections between stations, providing a network for each component of the magnetic field. We construct random surrogates of the data to determine the statistical significance of the individual network links. We find that the Pc2 in-phase undirected networks have the highest surrogate estimated signal-to-noise ratio (SNR) over most of the event and hence we focus on these. Here, undirected in-phase network connections are obtained when the maximum of the cross-correlation between Pc2 waveforms is at close to zero cross-correlation lag. Finally, we parameterize the global spatio-temporal correlation patterns using a few network parameters.

The paper is organized as follows. Section 2 summarizes the event studied, the available data, and the methodology for constructing the networks and network parameters that characterize specific spatial properties of the networks. Results in Section 3 show how these network parameters characterize the time-evolution of the St. Patrick's Day storm. We conclude in Section 4. Additional results and detailed methodology are shown in the appendix.

2. Methods

2.1. Geomagnetic Storm and Data

We focus on the 2015 St. Patrick's Day event (Wu et al., 2016) which occurred on the 17 March 2015. The time-dependent networks for this event are constructed from the full set of 128 ground magnetic field observations with 1 s cadence, curated by the SuperMAG and Intermagnet ground magnetometer collaborations. For our analysis we use the SuperMAG data calibration, ensuring magnetometer data have been preprocessed identically and allowing for multi-event and single event statistical analyses (Gjerloev, 2012). The vector time series for our data are given in coordinates where $\hat{n}$ is local magnetic north, $\hat{e}$ is local magnetic east and $\hat{z}$ is vertically down.

We use 1 s data from SuperMAG (Gjerloev, 2012) and Intermagnet (Kerridge, 2001) collaborations of ground-based magnetometers. The SuperMAG derived higher spatio-temporal resolution equivalents to the disturbance storm time (Dst) and auroral electrojet (AE) indices, SuperMAG electrojet (SME), and SuperMAG ring current (SMR) indices (Newell & Gjerloev, 2012) are used in this paper. The SMR index is calculated from all available ground magnetometer stations at geomagnetic latitudes between −50° and +50° (≈100 stations). For SMR values by magnetic local time (MLT) sector, magnetometer stations are used from four equally sized MLT regions and are defined with centers at 00, 06, 12, 18 in MLT (Newell & Gjerloev, 2012). The SME index is calculated from all available ground magnetometer stations at geomagnetic latitudes between +40° and +80° in the SuperMAG network (≈110 stations). For the solar wind parameters, we use OMNI data (Papitashvili et al., 2014) obtained from the SuperMAG website, which do contain gaps due to instrument outages during the 2015 St. Patrick's Day storm between 06:55–09:00 UT.

The 2015 St. Patrick's Day storm is the largest geomagnetic storm of solar cycle 24 (Li et al., 2017), classified as "Severe" on the National Oceanic and Atmospheric Administration geomagnetic storm scale (Jacobsen & Andalsvik, 2016; Poppe, 2000). The onset or SSC occurred around 04:45 UT on 17 March, when a CME reached the Earth. Initially, the IMF B_z component was northward, reaching ∼27 nT at SSC, then turned southward at around 06:00 UT. The storm reached its peak intensity at ∼00:00 UT on 18 March with minimum disturbance storm time index (Dst), ∼−223 nT and had recovered (reaching background) on the 25 March (Nosé et al., 2012; Wu et al., 2016).

The dynamical Pc2 wave network of cross-correlation is obtained over an 8 hr time window starting just before onset at 4:00 UT and ending at 12:00 UT, on the 17 March. Other studies have analyzed the response to the 2015 St. Patrick's Day storm using information theory techniques (Balasis et al., 2018), while others have observed the ionospheric response (Astafyeva et al., 2015).

2.2. Building a Dynamical Pc Wave Cross-Correlation Network

A network graphs the connections (edges) between entities (nodes). Examples include social media networks, where nodes are people and edges are friendships between them, and airline networks, where the nodes are airports and edges are flight paths (Newman, 2018). Network edges can be directed (flight path) or undirected and have connections with different weights. In a dynamical network, both the available nodes, and the connections between them, are time-varying. Here, the network will be built upon the cross-correlation between the observed magnetic field at pairs of ground-based magnetometer stations. A pair of stations are connected when the cross-correlation estimated in a moving time window exceeds a fixed threshold. For real-world systems, the appropriate threshold is uniquely determined for each application. Key properties of the network can be captured by time-varying network parameters, which then track the evolution of the geomagnetic storm in terms of cross-correlation between spatially distributed stations. This study extends previous work that used 1 min data (Dods et al., 2015, 2017; Orr et al., 2019, 2021a) to high-resolution (1 s) SuperMAG and Intermagnet data applied to Pc2 waves.

A detailed description of how the network is constructed is given in the appendix, and is summarized here. Each magnetometer time series is sampled using a moving 100 s long time window which is 10 times the largest Pc2 wave period. Consecutive windows overlap by half the window size (50 s). The Pc2 waveforms are then extracted by band-pass filtering the windowed time series of each magnetometer. The two waveforms from pairs of magnetometers are then cross-correlated using a normalized time-lagged-cross-correlation (see Appendix A1 in Appendix A). Next, a peak finding routine determines all positive and negative extrema of the cross-correlation

function (which oscillates about zero) and gives the amplitude of the peak closest to zero lag, A_{p_0} occurring at lag τ_{p_0}. If the absolute value of A_{p_0} is above a threshold such that the $|A_{p_0}| > 0.3$, the station pair are connected in the network. This procedure is repeated for all station pairs in each time window to generate the network. The threshold for the cross-correlation is set at 0.3, this threshold was obtained from test data of two sinusoidal signals superimposed with increasing amplitudes of white noise.

Each network edge falls into one of three categories depending on A_{p_0} and τ_{p_0}: (a) undirected in-phase, if $|\tau_{p_0}| \leq 1$ and $A_{p_0} > 0$. (b) Undirected anti-phase, if $|\tau_{p_0}| \leq 1$ and $A_{p_0} < 0$. (c) Directed, if $|\tau_{p_0}| > 1$. The maxima of the signed correlation peak closest to zero and sign of the lag at the correlation peak is used to determine the type of network edge. We find the largest extremum value close to zero as this allows us to find a lag which we can use to find the relative phase difference between the two waveforms. In our analysis we do not use the global maximum as this would select the lag at which the wave packet envelopes are coherent, not the oscillations within the envelope. These categories correspond to three distinct sub-networks which can exist at the same time. In Section 3 we will focus on the undirected in-phase network, and examples from the anti-phase undirected networks are given in Appendix B.

For each network category, there will then be a network for each magnetic field component, $\hat{e}$, $\hat{n}$, and $\hat{z}$, where $\hat{n}$ is local magnetic north, $\hat{e}$ is local magnetic east and $\hat{z}$ is vertically down (Newell & Gjerloev, 2012).

To test the statistical significance of network links, we will compare our analysis to a Pc2 surrogate dynamical network. We construct surrogate time series to test against the null hypothesis of no coherent phase information (Lancaster et al., 2018; Schreiber & Schmitz, 2000). Since our analysis relies on cross-correlation of band-passed signals, we test against the null hypothesis that one of the band-passed signals is not oscillatory. For each pair of stations, one windowed band-passed signal is randomly shuffled, and the other is unchanged. This excludes the possibility that a short-duration, band-passed colored noise signal can result in an oscillatory sample. The full network analysis is then performed on this surrogate pair to give a randomized surrogate network. The number of connections in each network divided by the number of randomized surrogate connections to then provide a surrogate estimated SNR $\phi_k(t)$, for each field component $k = \hat{n}, \hat{e}, \hat{z}$ at time, t.

2.3. Sub-Networks and Network Parameters

The overall evolution of each network can be tracked with network parameters, which in turn track different aspects of the evolution of the storm. These parameters will be defined for the networks for each magnetic field component, $k = \hat{n}, \hat{e}, \hat{z}$. Sub-networks, that is, subsets of the connections within the network, track different geographical and physical aspects of the magnetospheric response to the storm. The ratios of the number of connections in these sub-networks then parameterize the network structure.

The number of connections in each of the sub-networks is as follows:

- **Overall level of global activity, $\theta_k(t)$**: The total number of connections in the network, normalized to the total possible number of connections.
- **Localized in longitude, $C_k(t)$**: Number of connections between stations within two degrees of magnetic longitude are referred to here as being part of the same magnetometer "pseudo-chain", these signify resonance between different L-shells. We choose two degrees of magnetic longitude to ensure stations within 200 km or less (in the E-W direction) are counted as part of the same pseudo-chain. Magnetometer pseudo-chains can be within or between hemispheres. Magnetometer pseudo-chains have historically been used for Pc wave studies (Chisham & Orr, 1997; Rasinkangas et al., 1994; Ziesolleck & McDiarmid, 1994). We examined the stricter condition of magnetic conjugacy for resonance along a single field line. However, only two conjugate station pairs were found, compared with the 99 station pairs that could exhibit cross-correlation with one other station along the same pseudo-chain.
- **Globally resonant L-shells, $G_k(t)$**: The number of connections between stations in the geomagnetic northern and southern hemispheres. There are 29 stations in the southern hemisphere out of the 128 stations in total.
- **Short-range ($S_k(t)$) versus long-range ($L_k(t)$) in MLT**: The number of connections spanning ΔMLT < 4 hr are denoted as $S_k(t)$ and ΔMLT > 4 hr as $L_k(t)$. Any sub-network of multiple short-range connections will preferentially be found on spatial scales with ΔMLT < 4 hr, and as such can only exist within continental scales, that is, over a land-mass that is well populated by ground based magnetometers. Long-range connections on the other hand can be ocean-spanning and reach between continents. This network parameter then

discriminates between these two distinct classes of network connection. The extent in MLT is chosen such that it approximately corresponds to continental scales. We anticipate a local response to be dominated by the high density of magnetometers, here in North America and Canada.

- **Within the northern hemisphere, $N_k(t)$**: A regionally localized response on a single hemisphere will respond to high latitude convection and current systems. We focus on connections limited in extent to the geomagnetic northern hemisphere as it is more extensively sampled.

We will consider dimensionless ratios of the above network parameters, including north-south connections relative to magnetometer pseudo-chains connections G_k/C_k, in order to determine whether the response is dominated by local or global L-shell resonance. North-south connections relative to northern hemisphere connections, G_k/N_k will determine whether the response is local (confined to the northern hemisphere) or global. Finally, long-range connections relative to short-range connections L_k/S_k will show whether connections ΔMLT < 4 hr or ΔMLT > 4 hr dominate. The number of connections in each of these sub-networks is plotted as a function of time in Figure 1, and their ratios, the network parameters, are plotted in Figure 2.

3. Results

We first detail the timeline of the 2015 St. Patrick's Day storm and identify the time intervals when there is a high surrogate estimated SNR in Section 3.1. We then present the detailed network response as seen in the storm timeline and provide detailed snapshots of the network at key times in Section 3.2. We found that the dominant network is the in-phase undirected network for the $\hat{n}$ component. At peak, this network has ~5,000 connections compared to the ~1,000 connections in the $\hat{e}$, $\hat{z}$ in-phase undirected networks. The $\hat{n}$ undirected in-phase network has a high surrogate estimated SNR ($\phi_n > 25$) post storm onset. Therefore, we focus on the undirected in-phase network $\hat{n}$ component, and the $\hat{e}$, $\hat{z}$ components when the surrogate estimated SNR is high ($\phi_{e,z} > 25$). The sub-networks and network parameters do not necessarily track each other, or the Pc2 wave power.

3.1. Time Evolution of the Event

Figures 1 and 2 provide an overview of the storm, and the network parameter response. The format of these figures is as follows. Panel (a) summarizes the solar wind driving and panel (b) the overall magnetospheric response. The vertical lines indicate times ($T1$–$T6$) which sample each phase of the storm, for which we will plot snapshots of the detailed network response in Figures 3–8. Panel (c) plots the average Pc2 wave power over all magnetometer stations and the normalized total number of connections θ_k for $k = \hat{n}, \hat{e}, \hat{z}$. Panel (d) plots the surrogate estimated SNR ϕ_k constructed as detailed in Section 2. A higher the value of ϕ_k indicates a larger number of network connections relative to those in the surrogate time series. We have set the threshold for significant Pc wave activity relative to the level seen before onset, as detailed in Appendix A. Before onset, the number of network connections is therefore low, (<100) so that ϕ_k fluctuates rapidly about this threshold. The first significant network response is seen at onset.

The phases of the storm and the overall response of the network are shown in Figure 1 and are as follows:

- ***T*1, onset at 04:47:50 UT**: We see that IMF B_z increases to ~+27 nT in panel (a) as we see a sharp increase in SME and SMR by MLT sector in panel (b). However, the dynamic pressure applied by the solar wind (panel (a), black line) increases shortly after at 5:00 UT. Network connections for the $\hat{n}$, $\hat{e}$ and $\hat{z}$ components become significant as $\phi_n \approx 85$, $\phi_e \approx 35$ and $\phi_z \approx 15$. There is a sharp spike in all sub-networks.
- ***T*2, within 04:47:50–06:00:00 UT**: There is a day-side response with solar wind driven compression and IMF $B_z > 0$. Between $T1$ and $T2$, $\phi_n \approx 60$ on average, a significant response in the $\hat{n}$ component of the magnetic field. The network response in the other components is much less significant as there is a low number of connections (<100) in these networks.
- ***T*3, within 06:00–06:45 UT**: The IMF turns southward at 06:00 UT and there is an interval of $B_z < 0$. This can be expected to drive polar cap convection and we see a high latitude response begin in SME. All magnetic component sub-network connections increase after 06:10-06:20 UT, and now all components have a high surrogate estimated SNR with $\phi_{n,e,z} > 25$. This 10–20 min delay is consistent with that found previously for the ionospheric response to a southward turning of the IMF (Dods et al., 2017; Todd et al., 1988).
- ***T*4, 06:47:00 UT**: IMF B_z turns toward zero at $T4$ where the Pc2 wave power peaks and all components continue to have a high surrogate estimated SNR, $\phi_{n,e,z} > 25$. The sub-network responses peak earlier than the

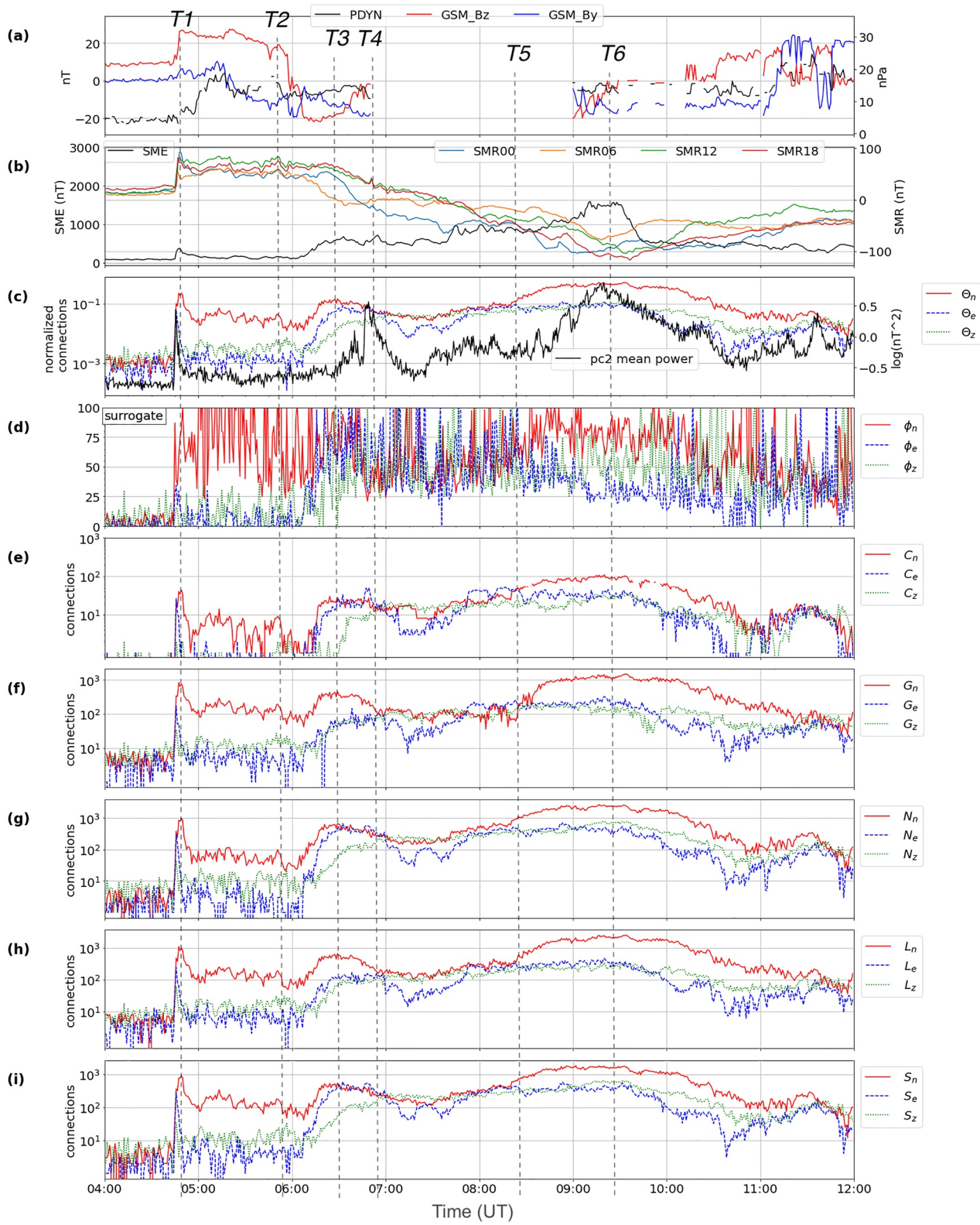

Figure 1.

Pc2 wave power, instead tracking the increase in SME, it levels out then decreases to a minimum about 20 min after the IMF reaches zero (however there is a data gap in the IMF after $T4$).

- ***T5–T6*, between 08:17:00–09:15:00 UT**: All magnetic component network connections increase and the surrogate estimated SNR remains large, while SME increases and SMR values by MLT sector decrease. All sub-network responses and the Pc2 wave power peak at the maximum excursion of SME and SMR. This is where magnetospheric and ionospheric current systems are responding most strongly to the storm. However, the network response, particularly for the $\hat{n}$ component of the field, starts to increase at $T5$ which is before the Pc2 wave power starts to increase, about an hour before the peak in the Pc2 power reaches its highest value of 2.4 nT.

Figure 1 shows that the in-phase instantaneous (close to zero cross-correlation lag) connections are at a high average surrogate estimated SNR post onset. Anti-phase connections are also significant at some times during this event, and these time intervals are shown in Appendix B in Figures B1 and B2.

3.2. Detailed Network Response, Network Parameters

Figure 2 panels (e–i) plot the network parameters, that is, ratios of the number of connections in the sub-networks from Figure 1. Snapshots of the networks at times $T1$–6 are plotted for the $\hat{n}$ magnetic field component network in Figures 3–8. Snapshots for the $\hat{e}$ and $\hat{z}$ component networks are given in the appendix, Section C, where these networks have different behavior and have sufficiently high SNR. The network snapshots plot all connections (green) and three of the sub-networks: (a) localized in MLT, where $\Delta\text{MLT} < 4$ hr (orange), (b) localized in MLT and between the geomagnetic north and southern hemispheres (purple), (c) along lines of fixed MLT (blue) showing magnetometer pseudo-chain connections which include magnetically conjugate connections. In Figures 3–8, panels (a) and (c) show the connections within each hemisphere, panel (d) shows all connections in geomagnetic coordinates, and panel (b) the degree distributions of the sub-networks (a–c). The nodes (magnetometer stations) are indicated by red circles in all panels. In Figures 3–8 the size of the (red filled) circle at each node in the network is scaled by the total number connections at that node. Black nodes indicate magnetometer stations that are not part of the network (no significant station-station cross-correlation).

The spatial coverage of magnetometer stations is not uniformly distributed, so that sampling varies with MLT. At storm onset, North America/Canada is initially located between dusk and close to midnight, while Europe is initially near dawn and Australia/East-Asia is just after noon. Europe then moves to the day-side while Australia/-East-Asia moves toward dusk, and North America/Canada moves through the night-side. Europe is dominated by the European quasi-Meridional Magnetometer Array chain (Del Corpo et al., 2020) and Australia/East-Asia dominated by the MAGDAS chain (Yumoto, 2006). Multiple chains are located across North America. Therefore, we expect to see a night-side response (AE) in North America/Canada, with a day-side response initially at Australia/East-Asia and then in Europe. The short-range MLT (orange/purple) and pseudo-chains (blue) connections will be dominated by these continental groups of magnetometers. The network snapshots (Figures 3–8) can give us a unique overview of how these different magnetometer groups are responding within and between each geographical region.

We now detail the in-phase network dynamics of the 2015 St. Patrick's Day storm using network parameters in Figure 2 (for significant components) which we compare to network snapshots in Figures 3–8 for the $\hat{n}$ component for each time, $T1$–6.

3.2.1. Time Interval *T*1, Onset, IMF $B_z > 0$, Pc2 Power Peak

Network parameters (Figure 2): Geomagnetic indices SMR values by MLT sector and SME spike (panel (b)) due to the pressure pulse from the solar wind, as does the Pc2 wave power and network response. There is a rapid increase in north-south connections relative to magnetometer pseudo-chains and northern hemisphere connections $G_{n,e}/C_{n,e} > 1$, $G_{n,e}/N_{n,e} > 1$ in panels (f) and (g). We also see that long-range connections dominate short-range connections with $L_{n,e}/S_{n,e} > 1$, indicating a global response, shown in panels (i) and (j). This confirms

Figure 1. Event overview and sub-networks. Panel (a), solar wind parameters, dynamic pressure (PDYN in black), geocentric solar magnetospheric coordinates IMF B_z (red), and B_y (blue) with data gap in OMNI data between ~ 6:55–9:00 UT. Panel (b), geomagnetic indices SuperMAG electrojet and SuperMAG ring current by magnetic local time sector. Panel (c), mean Pc2 power along with the normalized total connection number Θ_k for $k = \hat{n}, \hat{e}, \hat{z}$ (red, blue and green) magnetic field components. Panel (d), surrogate estimated SNR ϕ_k. Panel (e), the number of connections in a magnetometer chain (C_k). Panels (f) and (g), the number of connections in the geomagnetic northern hemisphere (N_k) and connections between the geomagnetic northern and southern hemispheres (G_k). Panels (h) and (i), connections spanning $\Delta\text{MLT} < 4$ hr (S_k) and spanning $\Delta\text{MLT} > 4$ hr (L_k). Reference times are labeled $T1$–6 for which network snapshots are shown in Figures 3–8.

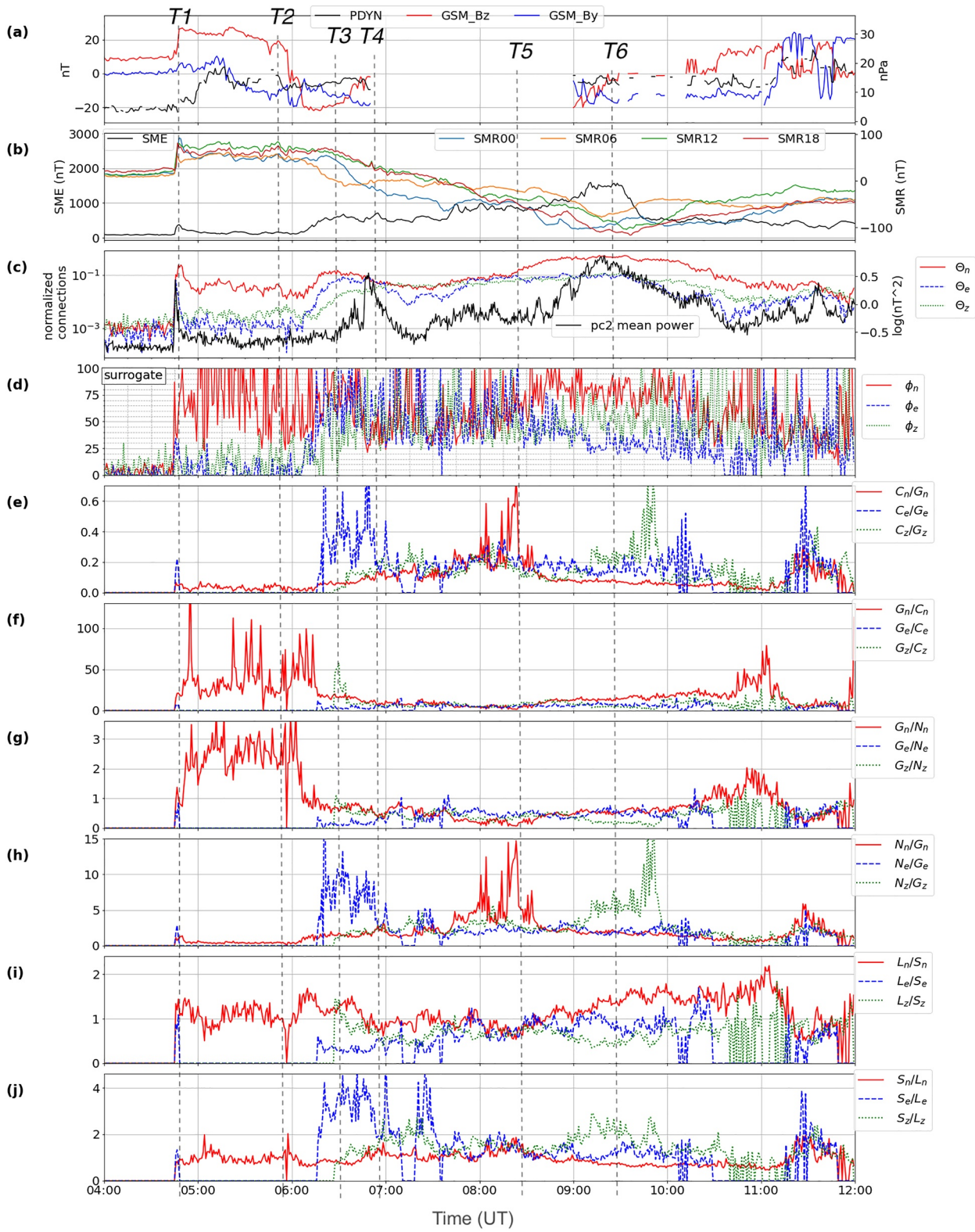

Figure 2.

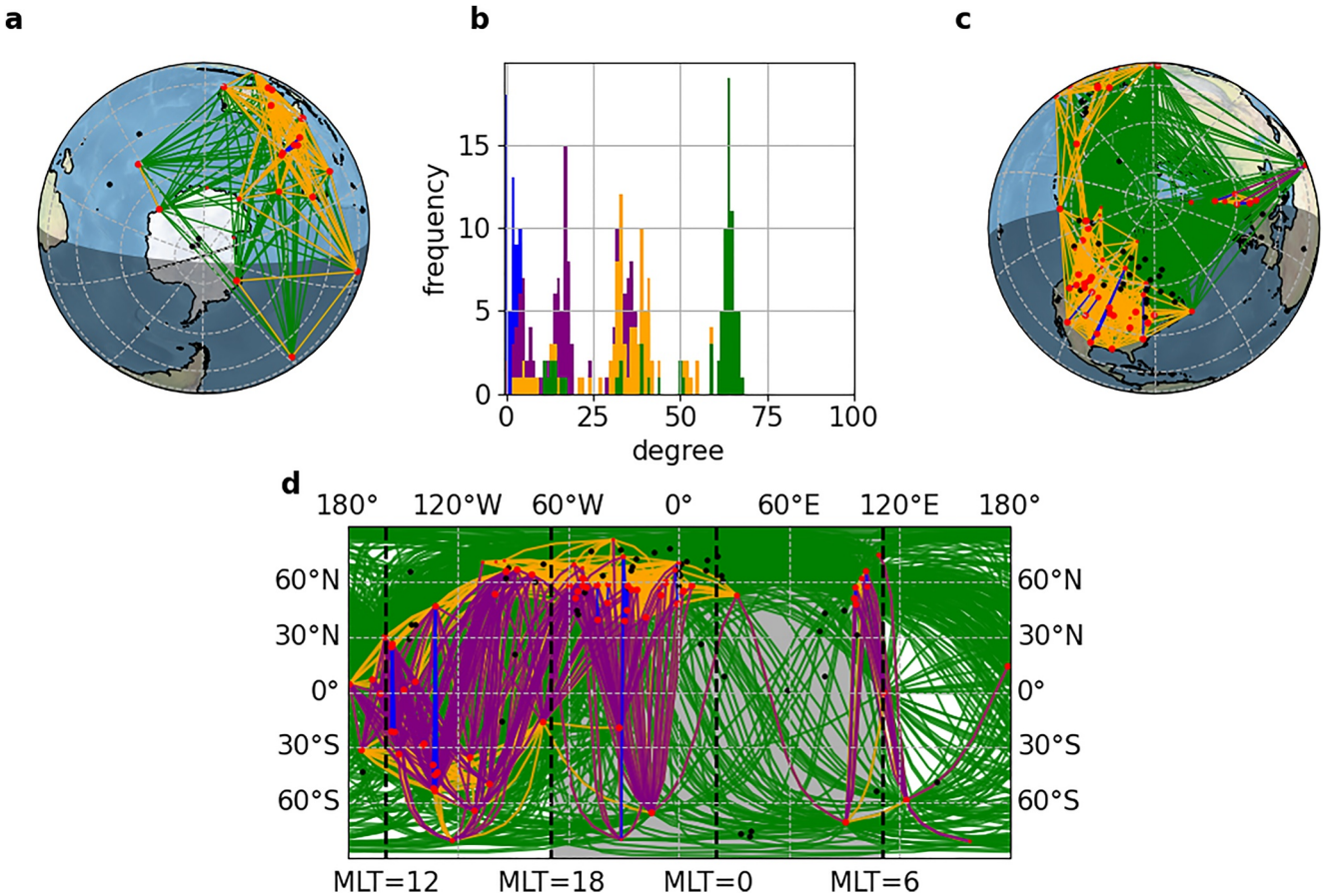

Figure 3. Network snapshot at *T*1 (04:47:30 UT) for the $\hat{n}$ magnetic field component comprising 81 stations. Throughout panels (a)–(d), four groups of connections are shown, all connections (green), superimposed are connections within ΔMLT < 4 hr (orange), north-south connections with ΔMLT < 4 hr (purple), and pseudo-chains (blue). Panel (d) shows connections plotted in geomagnetic coordinates. Panels (a) and (b) show connections plotted in geographic coordinates and limited to the southern and northern hemispheres respectively. The global degree distribution for the given network snapshot is shown in (b) with colors corresponding to network edges in panels (a), (b), and (d).

that the enhancement in SME is due to the sudden commencement of the storm, rather than an electrojet response. We also see that north-south ($G_{n,e}$) connections are enhanced as $B_z > 0$ showing global L-shell resonance due to the solar wind pressure pulse and shear flow at the flanks.

Network snapshot (Figure 3): A global response is seen with long-range connections across the globe and short-range MLT connections excited in all three magnetometer groups. There are relatively more connections on the day-side (hence connected nodes) and at all latitudes. On the night-side there are more connections at higher latitudes (>30°) with a corresponding gap in yellow connections between 0 and 6 hr in MLT. Pseudo-chains are excited, particularly on the day-side, including two conjugate connections one on the day-side and one on the night-side. The degree distributions in panel (d) show that sub-networks are distributed broadly and are peaked showing distinct groups. Overall the network response is consistent with sharp day-side compression of the magnetosphere.

Figure 2. Event overview and network parameters. Panels (a)–(d) are as in Figure 1. Panels (e)–(j), evolution of the undirected in-phase $\hat{n}$, $\hat{e}$, and $\hat{z}$ component network parameters which are ratios of the number of connections in the sub-networks discussed Section 2.2 and their inverses. Panels (e) and (f), ratios between connections in northern and southern geomagnetic hemispheres (G_k) and magnetometer pseudo-chains (C_k). Panels (g) and (h), ratios between connections in the geomagnetic northern hemisphere (N_k) and connections between the geomagnetic northern and southern hemispheres (G_k). Panels (h) and (i), the proportion of connections extending across ΔMLT < 4 hr (S_k) and ΔMLT > 4 hr (L_k). Parameters are only plotted if the network has more than 100 connections, otherwise a value of zero is given. Reference times are labeled *T*1–6 for which network snapshots are shown in Figures 3–8.

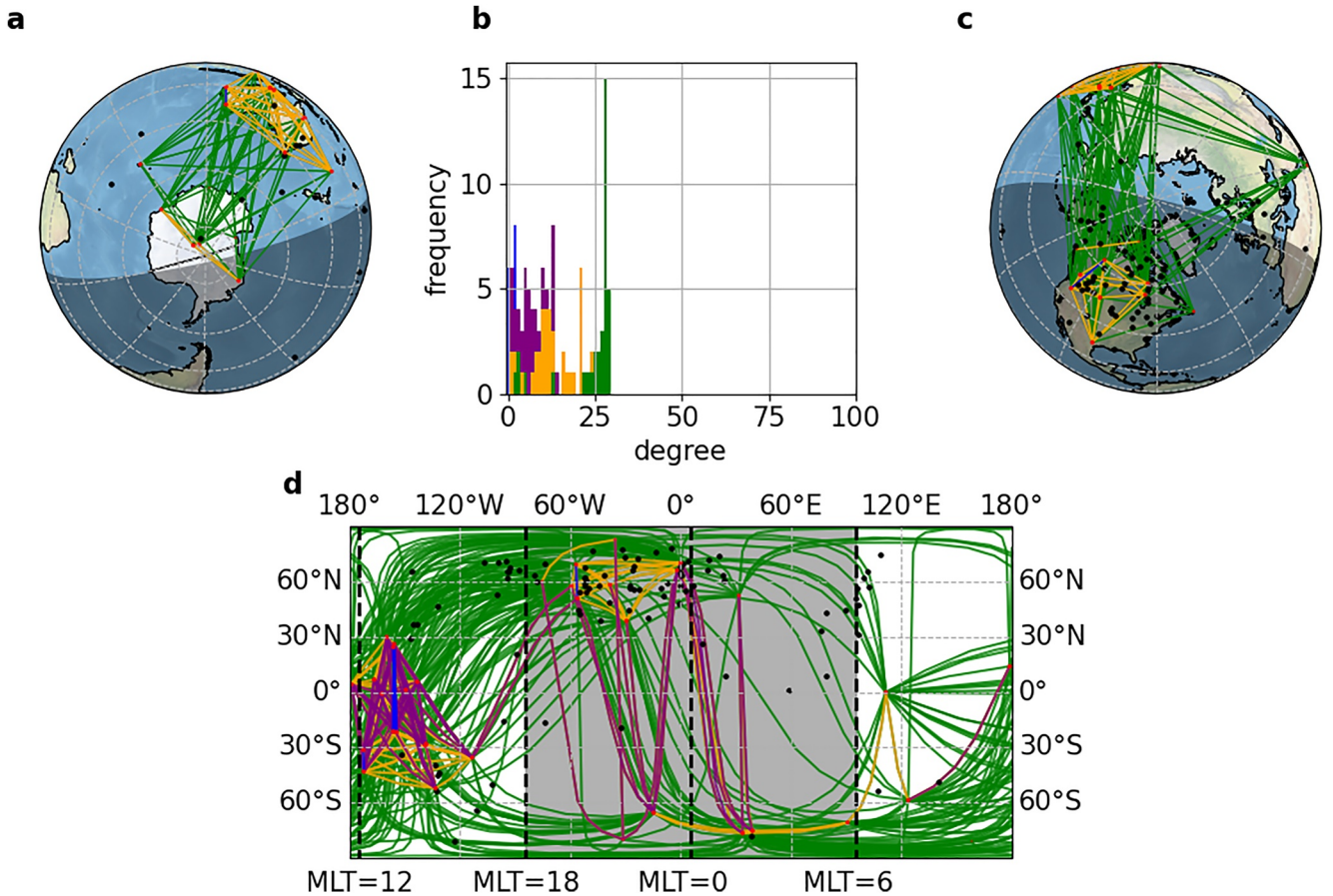

Figure 4. Network snapshot at $T2$ (05:50:00 UT) for the $\hat{n}$ magnetic field component network comprising 35 stations. The figure format is the same as in Figure 3.

3.2.2. Time Interval 04:47:50–06:00:00 UT Including $T2$, IMF $B_z > 0$

Network parameters (Figure 2): The number of north-south connections continues to exceed the number of magnetometer chain and northern hemisphere connections G_n/C_n, G_n/N_n both >1 in panels (f) and (g). At this time, long-range connections continue to dominate short-range connections, $L_n/S_n > 1$, panels (i) and (j).

Network snapshot (Figure 4): There are fewer stations in the network overall. Short range MLT connections and pseudo-chains are mainly on the day-side with only one chain excited in Canada. Most low latitude connections are on the day-side including Antarctic stations. North-south hemisphere connections remain elevated due to a day-side cluster (between 30°N and 60°S). The degree distributions in panel (d) show that all groups are shifted toward the left and narrowed, now having lower average degree values. The network response is consistent with day-side compression and $B_z > 0$, it is still the sudden commencement phase.

3.2.3. Time Interval 06:00–06:45 UT Including $T3$, IMF $B_z < 0$ to $B_z \approx 0$

Network parameters (Figure 2): During this phase, SME starts to increase, consistent with the onset of polar cap convection now IMF B_z and B_y are negative. As above, the detailed network response lags the IMF southward turning by approximately 15–20 min. The parameter $N_{n,e}/G_{n,e} > 1$ shows an increase in the number of northern hemisphere connections with the $\hat{e}$ component showing the greatest response. Magnetometer pseudo-chains (relative to north/south hemisphere connections) $C_{n,e}/G_{n,e} \approx 0.1, 0.3$ become enhanced, dominated by magnetometers in North America/Canada on the night-side. The local response is highlighted by short-range connections in MLT becoming dominant for the $\hat{e}$ component ($S_e/L_e > 1$). Long-range connections in MLT still persist in the $\hat{n}$ component with $L_n/S_n > 1$.

Network snapshot (Figure 5): The number of connections in the network has increased and we see degree distributions shifted to higher average degree in panel (d). There are more network connections both within and between

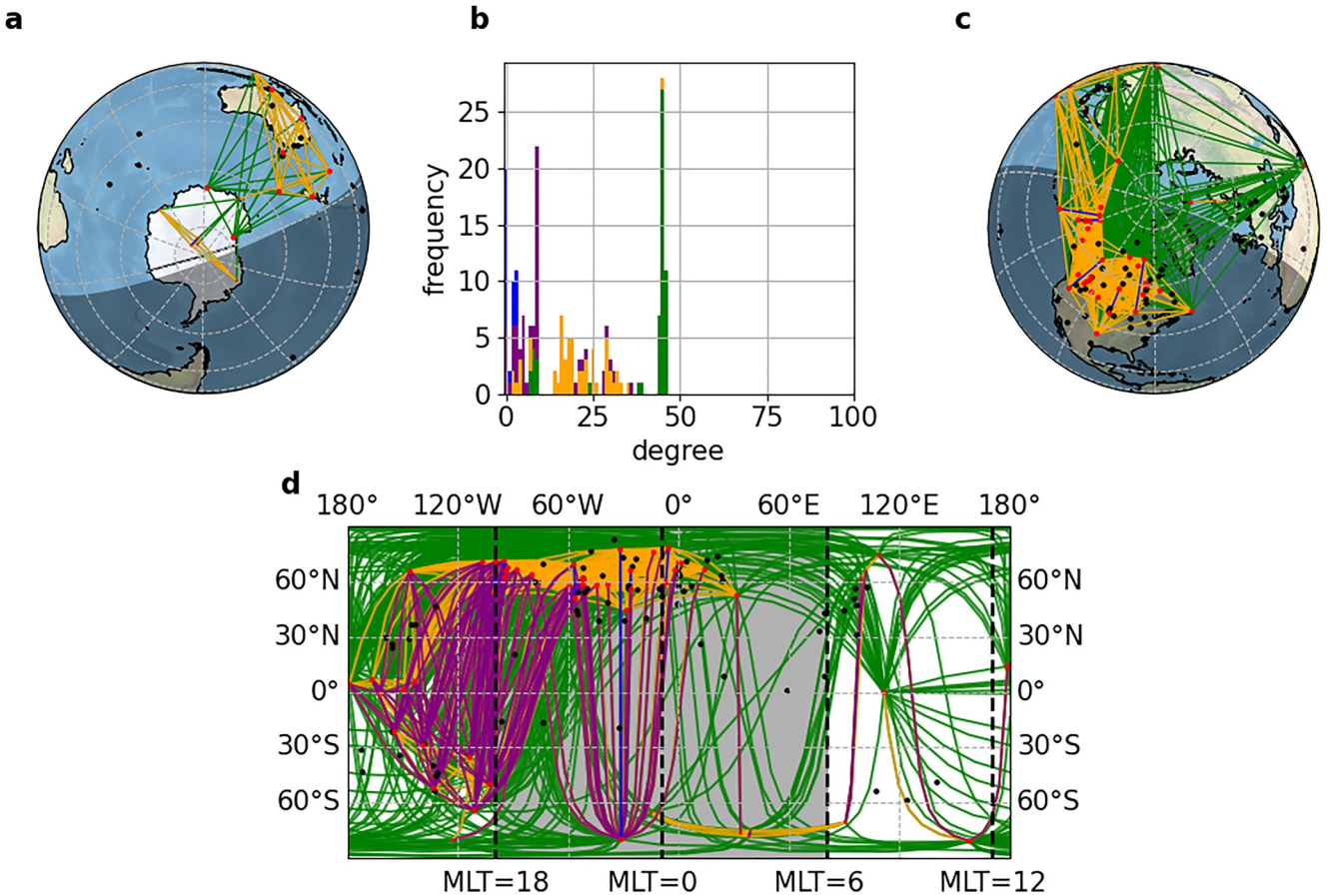

Figure 5. Network snapshot at $T3$ (06:20:00 UT) comprising 57 stations for the $\hat{n}$ component. The figure format is the same as in Figure 3.

high latitude stations on the dusk side, consistent with enhanced dusk side polar cap convection under conditions of IMF $B_y < 0$. Multiple pseudo-chains are now excited in North America/Canada and there is a single conjugate connection between the North and South Pole, while in the vicinity of the South Pole only a single chain is excited. The network response here shows increasing connections both across MLT and across north and south hemispheres within a 4 hr range of MLT, consistent with enhanced convection that is globally correlated during this interval of IMF $B_z < 0$ enhanced convection.

3.2.4. Time Interval $T4$, 06:47 UT, IMF $B_z \approx 0$, Pc2 Power Peak

Network parameters (Figure 2): At this time IMF $B_z \approx 0$, SME is at a similar level to $T3$, and the Pc2 power is enhanced. We see the number of long-range and short-range connections are similar as $L_n/S_n \approx 1$ while $L_z/S_z > 1$, panels (i) and (j). Northern hemisphere connections for the $\hat{e}$ component continue to be enhanced relative to all other connections. The compressional component $\hat{z}$ shows an increase in the relative number of northern hemisphere connections which peaks at $G_z/C_z \approx 100$ in panels (e) and (f).

Network snapshot (Figure 6): We see that Pc2 power reaches a similar value to that seen at $T1$, however, this time we see a predominately localized high latitude response at North America between latitudes 60°N and 90°N which highlights that the network response does not simply track Pc2 power. Pseudo-chains between hemispheres are mainly on the day-side, with few pseudo-chains excited on North America and a single chain in the vicinity of the South Pole. There are more MLT < 4 north-south connections on the dusk-side. The degree distribution here is similar to that at $T3$. Overall, the network response at this time is consistent with enhanced high latitude currents during SME enhancement.

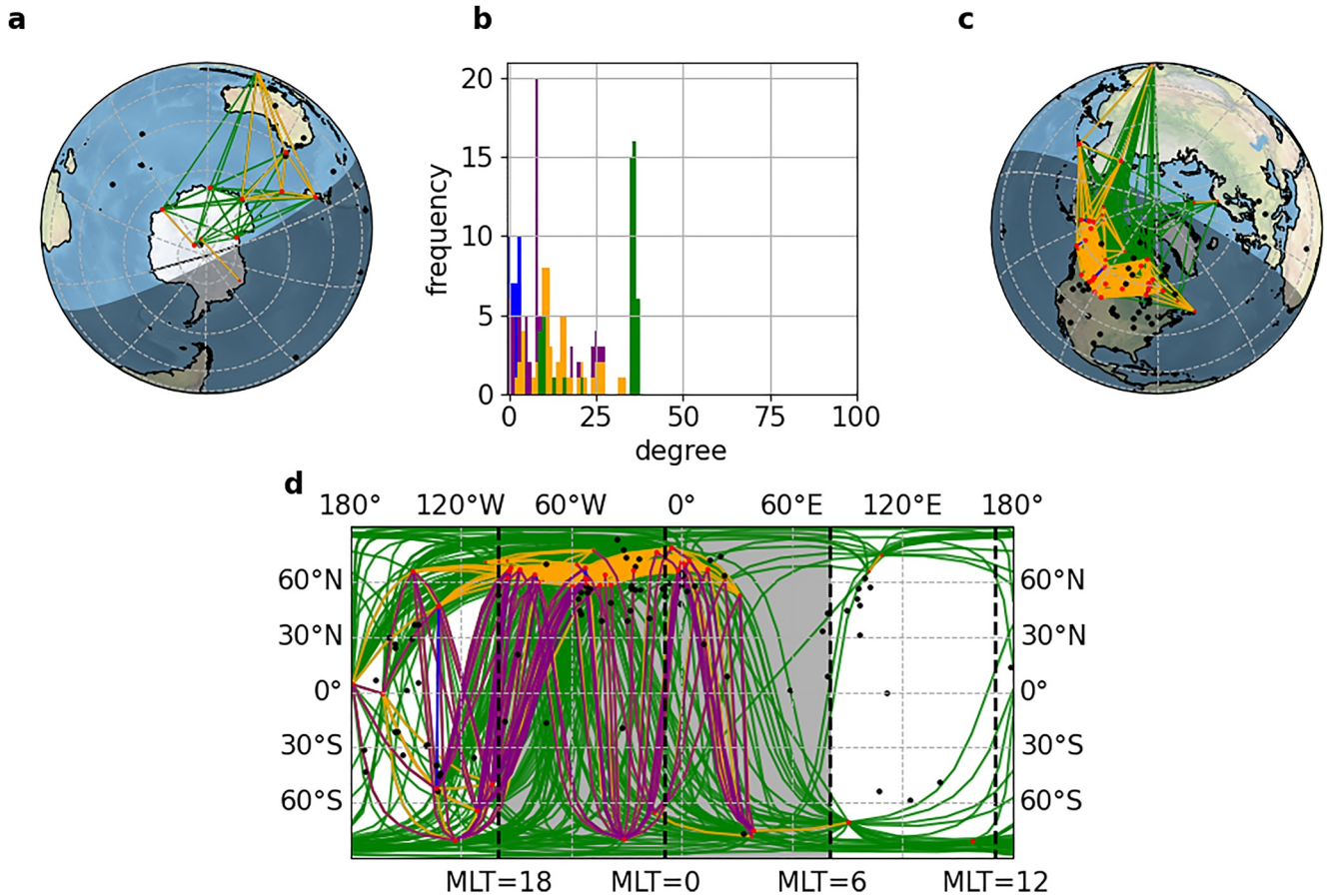

Figure 6. Network snapshot at $T4$ (06:45:50 UT) comprising 49 stations for the $\hat{n}$ component. The figure format is the same as in Figure 3.

3.2.5. Time Interval $T5$, 08:17 UT

Network parameters (Figure 2): Values for SMR values by MLT sector become more negative and SME increases to ≈1000 nT. There is a sharp peak in parameters C_n/G_n and N_n/G_n which reach values ∼0.5 and ∼10 respectively, in panels (e) and (h). These parameters indicate that network activity is becoming more localized in the northern hemisphere. This is the time when the network response for the $\hat{n}$ component of the magnetic field starts to increase, about an hour before the peak in Pc2 wave power occurs.

Network snapshot (Figure 7): Most connections are on the night-side at latitudes >60°N, consistent with high latitude ionospheric currents, such as the AE. Excited nodes are predominantly on the night-side and a few night-side pseudo-chains are also excited. The sparsity of connections between the north and south hemispheres is also reflected in the degree distributions, panel (d).

3.2.6. Time Interval 09:15–12:00 UT Including $T6$, IMF $B_z < 0$ to $B_z > 0$, Pc2 Power Peak

Network parameters (Figure 2): Enhanced magnetospheric convection resumes as IMF $B_z < 0$ while SME and Pc2 power peaks as SMR by MLT sector is close to minimum. At this time, long-range connections dominate with $L_n/S_n > 1$ and the total number of connections Θ_n peaks, indicating a global response. Later, at 09:50 UT convection slows as $B_z \approx 0$ and we see the compressional component (magnetic $\hat{z}$ component) parameters peak with $N_z/G_z \approx 15$ and $C_z/G_z \approx 2$ shown in panels (e) and (h). Next, B_z spikes reaching +17 nT at 10:30 UT as more north-south connections are seen when $G_n/N_n > 1$ and $L_n/S_n \approx 2.3$ reaching maximum at 11:05 UT, showing a global response similar to $T1$. Large fluctuations in B_y coincide with a peak in $C_e/G_e \approx 0.6$ at 11:30 UT. At this time there is no peak for N_e/G_e indicating that more magnetometer pseudo-chains are excited outside of the northern hemisphere, unlike previously seen at times $T3$ and $T4$.

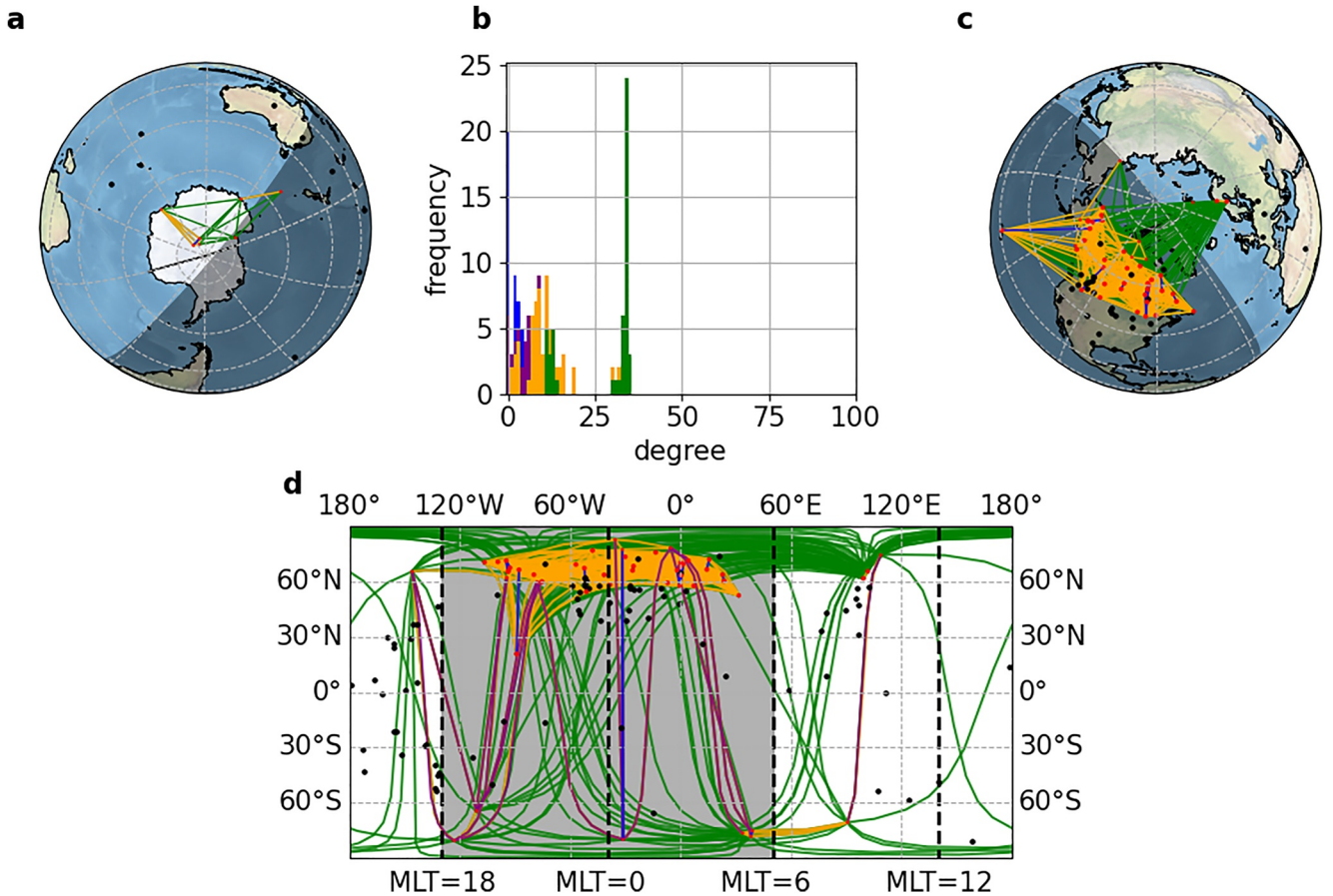

Figure 7. Network snapshot at *T*5 (08:18:20 UT) comprising 50 stations for the $\hat{n}$ component. The figure format is the same as in Figure 3.

Network snapshot (Figure 8): This is the peak of excitation, with activity at all latitudes. Pseudo-chains are excited in all MLT zones, noon-dusk, dusk-midnight, midnight-dawn, and dawn-noon. The two conjugate connections are on the day and night-side. There are more connections, in particular N-S connections and short-range connections at high latitudes, located in the region between midnight and dusk compared to the region between midnight and dawn. Again, this could simply reflect the available station coverage, but is also consistent with enhanced polar cap convection on the dusk side under conditions of IMF $B_y < 0$ (Moen et al., 2015). At this time, we see the network is the most highly connected seen in the entire event, the degree distributions are comparatively broader and the network has the highest average degree seen in the event. In the degree distributions, distinct groups can be clearly seen for connections limited to ΔMLT < 4 hr.

4. Discussion

There is a well developed literature of Pc wave studies focused on chains and geographically localized regions. One such example is the measurement of Pc1 and Pc5 waves during strong magnetospheric compression using the Combined Release and Radiation Effects satellite and Scandinavian magnetometer chains on the dawn-side (Liu et al., 2012; Rasinkangas et al., 1994). In this paper we propose a new framework, namely networks, to quantify the dynamics of the global ULF activity from the full set of 100+ ground based magnetometers. This approach provides both detailed visualization, and quantitative parameterization of both locally and globally coherent ULF activity and the relationships between them. This first study is of an event that has already been subject to detailed analysis, the 2015 St. Patrick's Day storm. We characterize the globally coherent dynamical response of the magnetosphere as seen in Pc2 waves, reducing 128 time series to a time series of a few key network parameters. The network parameters that we propose here complement traditional geomagnetic indices which are designed to monitor specific larger scale current systems such as the AE and ring current. This param-

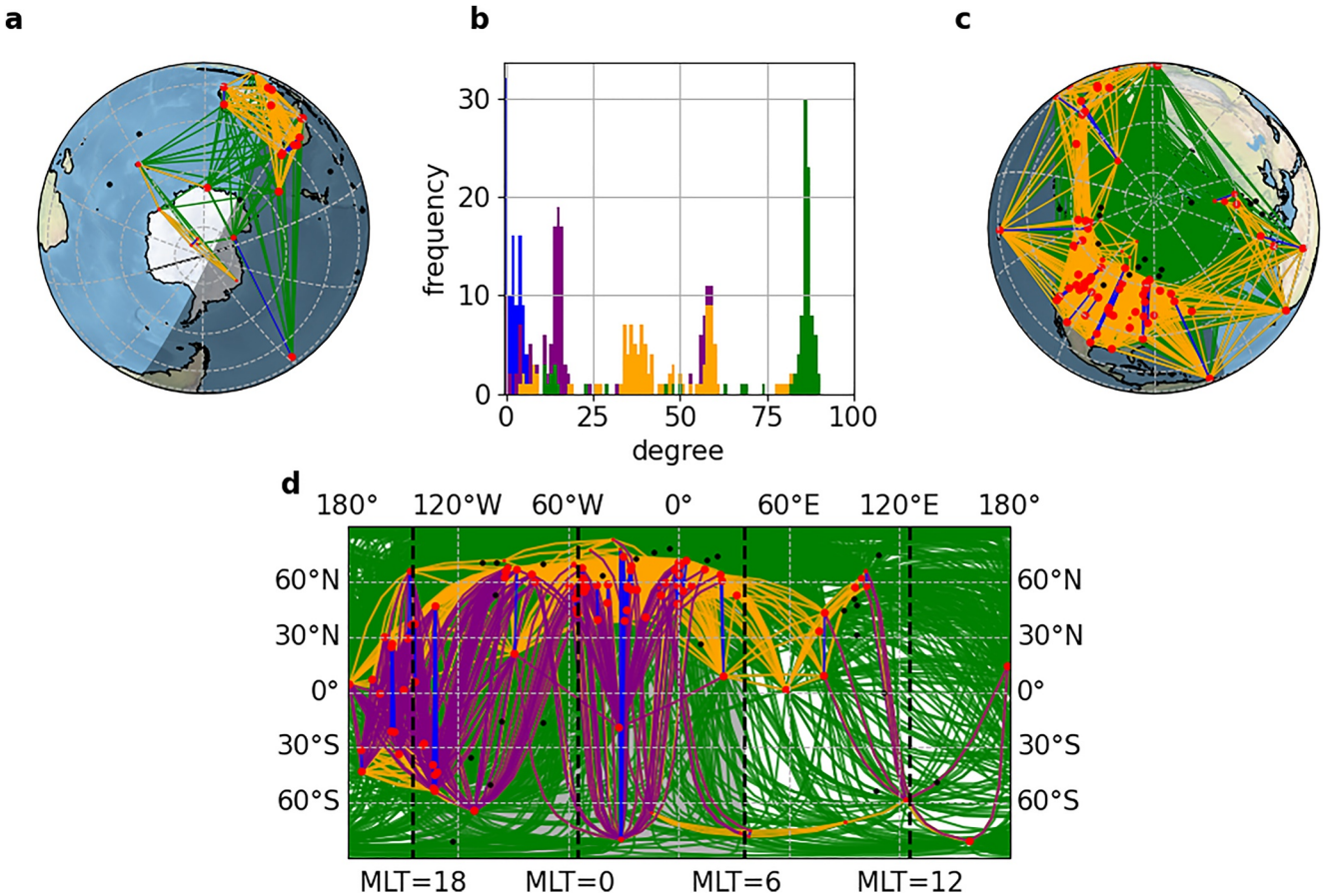

Figure 8. Network snapshot at $T6$ (09:15:00 UT) comprising 103 stations for the $\hat{n}$ component. The figure format is the same as in Figure 3.

eterization provides a starting point for quantitative comparative statistical studies across multiple events which can discriminate between model predictions (Orr, Chapman, Gjerloev, et al., 2021).

Previously, 1 min ground-magnetometer time resolution data has been used successfully to obtain the timings and structure of substorm current systems using network analysis techniques such as community detection (Dods et al., 2015; Orr et al., 2019, 2021a). Here, we construct the time dependent network using 1 s time resolution data which resolves the Pc wave response and captures the evolution of geomagnetic storms in greater dynamical detail. The Pc2 wave band has a period between 5 and 10 s (Jacobs et al., 1964) and is the highest frequency Pc wave band resolvable with 1 s data, minimizing the length of the corresponding time window over which cross-correlation is estimated to form network connections between station pairs. This particular analysis method is chosen w.r.t the physics at hand. We assume band-passing the time series data results in Pc waveforms that are a coherent waveform of several periods such that duration of these periods will not significantly vary over the waveform duration. We test this by requiring the average period of the cross-correlation function to be approximately equal to the average period of both waveforms, as shown in Appendix A2 in Appendix A, Figure A2, step (vi).

In order to access the significance of pairwise correlation, we have determined a benchmark (an effective SNR) using surrogate data. The surrogate is constructed by randomly shuffling one of each pair of windowed, band-passed signals before cross-correlation. We define this as a surrogate derived SNR which allows us to determine when the network parameters are significant. We anticipate that more information can be extracted from networks to test specific hypotheses, an example is community structure (Orr, Chapman, Gjerloev, et al., 2021). However, these would also need to be benchmarked against appropriate random surrogates.

We have focused principally on the $\hat{n}$ component, however networks are obtained for each of the magnetic field components, $\hat{n}$, $\hat{e}$ and $\hat{z}$ and these all respond at onset, but then behave differently throughout the storm. One clear example is seen in the sharp increase in northern hemisphere connections for the $\hat{e}$ component during SME

enhancement at time $T3$ in Figure 2, showing greater sensitivity to AE formation. The evolution of geomagnetic storms in terms of the global coherence of Pc waves has a direct relation to the physics of the system. Standing Pc wave mode structure depends on the length of the field line and whether foot points move anti-phase or in-phase to each other (Dai et al., 2013; Hudson et al., 2004). For the closed field lines of the Earth's magnetic dipole, oscillations in the geomagnetic $\hat{e}$ component are in the toroidal direction, in the $\hat{n}$ component, poloidal, and the $\hat{z}$ component, approximately compressional.

Other events analyzed include the 2013 St. Patrick's Day storm which we have not included in this work, but will form the basis of future work as part of a statistical study. We again find that the Pc2 in-phase networks have the highest surrogate estimated SNR for all magnetic field components over most of the event. We see a similar in-phase network and sub-network response at onset, however there are some deviations due to differences in solar wind driving conditions.

In this first study, we have shown that the instantaneous Pc2 networks that are constructed from the maximum of the cross-correlation at zero lag, can categorize key phases of the 2015 St. Patrick's Day storm. There is also information contained in the non-zero lag cross correlation, which can be used to track propagation of coherent Pc waves by building directed networks. This will be the topic of future work.

5. Conclusions

We have provided a single event network analysis of the 2015 St. Patrick's Day storm for an 8 hr time window around onset. In the above results, we have demonstrated that all major phases of the storm are captured in the network parameters, which, in turn, are derived from the dynamical networks of Pc2 activity.

In this paper, we present a new methodology to build networks that capture the spatial coherence of global Pc2 wave activity. The time dependent network is constructed from 1 s observations using 100+ ground magnetometers collated by SuperMAG and Intermagnet. Our results show that the evolution of the 2015 St. Patrick's Day storm can be parameterized from the spatial extent and level of cross-correlation of Pc2 waves. The most significant response to the storm is found in the undirected in-phase network, where the cross-correlation between Pc2 waveforms from pairs of magnetometers form peaks close to zero cross-correlation lag. However, the method has the potential to yield both undirected (cross-correlation lag close to zero) and directed (non-zero cross-correlation lag) networks corresponding respectively to an instantaneous and delayed, coherent response. We establish the statistical significance of our results by testing against randomized surrogate data.

We identify a set of time dependent network parameters for field components $k = \hat{n}, \hat{e}, \hat{z}$ which track the phases of the storm as it evolves. These are:

- $C_k(t)/G_k(t)$ which is the number of connections within a restricted range of magnetic longitude normalized to the number of connections between the geomagnetic north and southern hemispheres. This parameterizes excitation along pseudo magnetometer chains, that is, across resonant field lines at localized MLT compared to excitation globally across L shells.
- $G_k(t)/N_k(t)$ which is the number of connections between the geomagnetic northern and southern hemispheres normalized to connections in the geomagnetic northern hemisphere. This parameterizes local coherence versus global, L shell and closed field line spanning coherence and is also a flag for spatial undersampling, in this case the night-side response at high latitudes is seen for the St. Patrick's Day storm in the northern hemisphere as North America/Canada are located on the night-side.
- $S_k(t)/L_k(t)$ which is the number of connections between stations within $\Delta\text{MLT} < 4$ hr of each other normalized to the number of connections spanning $\Delta\text{MLT} > 4$ hr. This parameterizes excitation across magnetic L shells at a localized MLT compared to the excitation globally across L shells. It is also a flag for spatial undersampling as it compares within-continent, and potentially ocean spanning, connections.

These network parameters respond to all the distinct phases of the storm, the initial onset, response to subsequent southward and northward turnings of the IMF, and enhancement of magnetospheric current systems seen in geomagnetic indices. The network response is based on cross-correlation and does not simply track the Pc2 wave power. For example, we find a response to turnings of the IMF that are seen at 10–20 min delays, these precede enhancements in Pc2 wave power.

Once the network parameters are established, they can be used to make detailed quantitative statistical comparisons across many events. This can quantify how the detailed evolution of a geomagnetic storm depends on the history of the solar wind driving, and the past state of the magnetosphere. In future work, this analysis can in principle also be applied and compared between different Pc wave bands as different Pc wave frequencies are generated by and respond to different solar/magnetospheric interactions.

Appendix A: Building Dynamical Pc Wave Networks

Here we present the analysis process developed to build the dynamical Pc2 (or any other Pc wave) network in detail. The process requires two stages: (a) data preprocessing to extract the Pc2 waveforms from our raw data and (b) constructing the network from the cross-correlation matrix formed between all possible station pairs.

A1. Pc Waveform Extraction

Before we can build networks, the data is preprocessed to extract the Pc waveforms, we summarize these steps shown in Figure A1. For each magnetometer, a finite time interval is extracted at time t for a given magnetic field component, using a time window of $\left[t_k, t_k + 10T_{Pc_{\max}}\right]$, where $T_{Pc_{\max}}$ is the maximum value of the Pc wave period found in the window. Using a Tukey window in the time domain and overlapping successive windows such that time t is successively stepped by $t_{k+1} = t_k + 5T_{Pc_{\max}}$, minimizes spectral leakage. Time windows containing more than $T_{Pc_{\min}}/4$ of consecutive data gaps are excluded. The Pc wave mode is then extracted by band-pass filtering the Fourier transform (FT) of the windowed time series using the Butterworth filter (Butterworth, 1930) which has a frequency response which is relatively flat across the frequency band; we denote cutoff frequencies f_l, f_u (lower and upper frequency as 1/5 and 1/10 Hz) and central frequency f_0. The time-domain Pc2 waveform is then obtained by the inverse Fourier transform (IFT) (Jacobs et al., 1964).

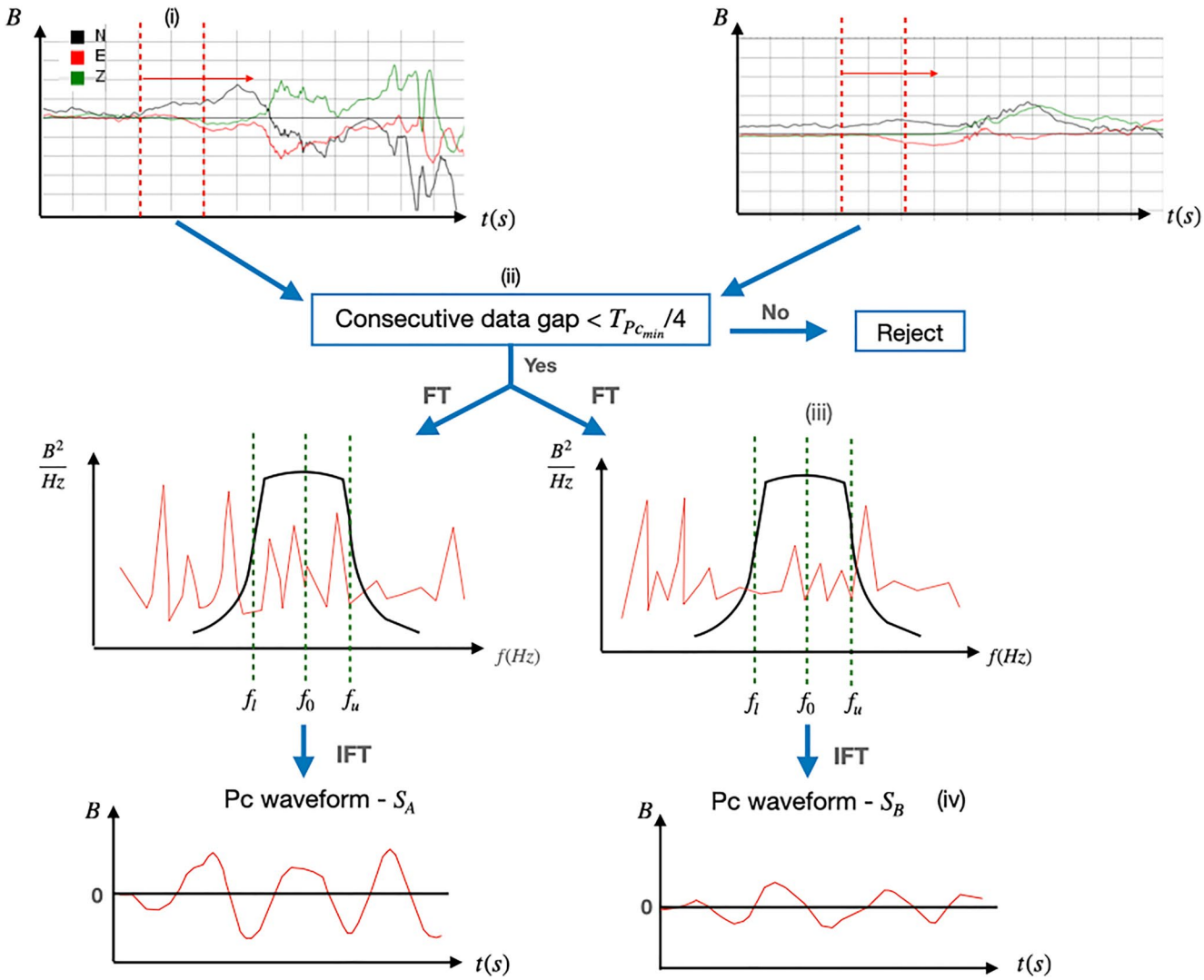

Figure A1. Pc waveform extraction flow chart. (i) Time window applied to a magnetic field component for two magnetometer station time series. (ii) If a time window has consecutive data gaps, reject and check the next pair of time windows. (iii) Fourier transform, then band-pass filter using a Butterworth filter for the desired Pc band. (iv) Inverse Fourier transform to obtain the Pc waveforms.

A2. Constructing the Network

We obtain the time-lagged cross-correlation function between pairs of Pc waveforms extracted at each t_k for each field component and for each magnetometer station pair. The cross-correlation is used to determine whether a network edge, or connection exists between the pair magnetometer stations at each sample time t_k. We impose both a cross-correlation noise threshold and a waveform test, which are used to reject pairs of Pc waveforms where the cross-correlation is not statistically significant, as discussed below.

Pc waveforms that are above the noise are oscillatory wave packets as they arise from a relatively narrow band-passed signal, the cross-correlation then oscillates as a function of lag, with the Pc waveform period. The lag τ_n, at which the cross-correlation has its maximum excursion, either positive or negative nearest to zero lag, indicates whether the network connection is undirected ($|\tau_n| \leq 1$) or directed ($|\tau_n| > 1$). Depending whether the waveforms are instantaneously in-phase or anti-phase, we assign either an in-phase or anti-phase undirected connection. Directed connections arise when the pair of waveforms are maximally coherent when one of the waveforms is phase lagged w.r.t to the other. The sign of the non-zero lag indicates which signal is in advance of the other, hence the network connection has a direction.

The complete procedure to build network connections using Pc waveforms is detailed in Figure A2: (i) the zero crossings of Pc waveforms S_A and S_B are used to determine the average periods T_{S_A} and T_{S_B} (ii) The background noise threshold is set as P_q, where P_q is the average quiet time power in the Pc2 wave band before onset. We require the peak values of both S_A and S_B to exceed this threshold. (iii) We obtain the cross-correlation between Pc waveforms S_A and S_B using the cross-correlation function (Pearson, 1896):

$$C_{X,Y}(\tau) = \frac{\sum_{t=1}^{N}\left(X(t)-\bar{X}\right)\left(Y(t-\tau)-\bar{Y}\right)}{(N-\tau)\sqrt{\frac{1}{N}\sum_{t=1}^{N}\left(X(t)-\bar{X}\right)^2}\sqrt{\frac{1}{N}\sum_{t=1}^{N}\left(Y(t)-\bar{Y}\right)^2}} \tag{A1}$$

the extrema of $C_{X,Y}(\tau)$ are determined using a standard peak finding routine. (iv) The threshold for the absolute value of the cross-correlation amplitude is set at 0.3, this threshold was obtained from test data of two sinusoidal signals superimposed with increasing amplitudes of white noise. (v) Checks that the signal has amplitude which decays slowly relative to the waveform periods such that there is at least one positive and negative peak above the cross-correlation threshold. (vi) Requires the average period of the cross-correlation function to be approximately equal to the average period of both waveforms, within a tolerance factor of 1.6, ensuring the period of the Pc2 waveforms does not drift. Steps (iv, v, vi) mitigate cross-correlation due to time non-stationary. (vii) Determine the amplitude A_n and lag τ_n of the cross-correlation peak closest to zero lag. (viii) A network connection (edge) is assigned between the two magnetometer stations for the time window used to obtain Pc waveforms, S_A and S_B. The type of connection is determined from the properties cross-correlation peak amplitude A_n and lag τ_n. If $|\tau_n| > 1$, the network connection is directed, the direction is determined by the sign of lag τ_n. Otherwise if $|\tau_n| \leq 1$ and $A_n > 0$ the network connection is in-phase and undirected, whereas if $A_n < 0$ the network connection is anti-phase and undirected.

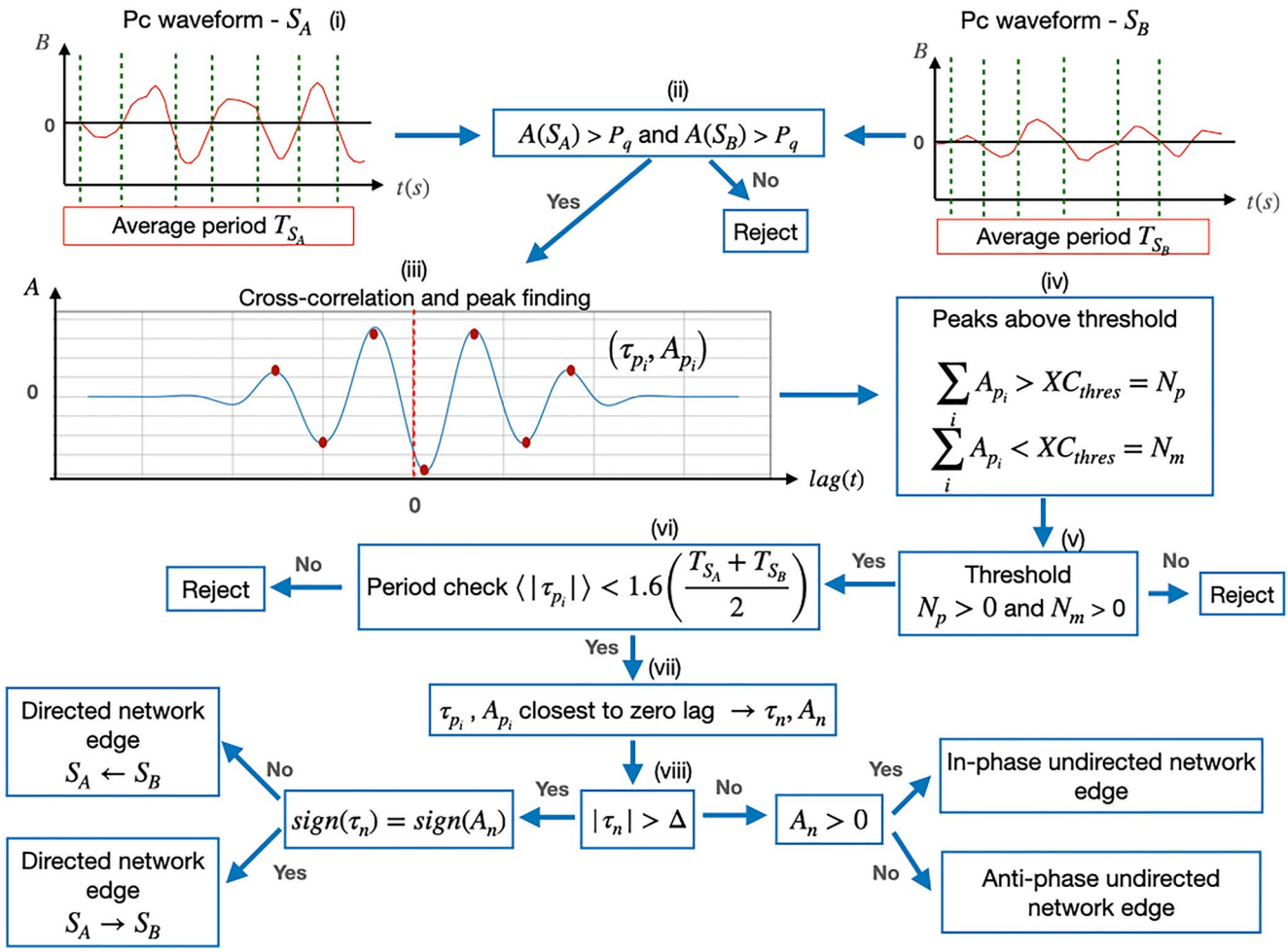

Figure A2. Network edge building flow chart. (i) Determine the average Pc waveform periods T_{S_A} and T_{S_B}. (ii) Reject Pc waveforms with amplitude below the average storm pre-onset levels. (iii) Obtain the cross-correlation between Pc waveforms S_A and S_B and find the extrema. (iv) Test the cross-correlation extrema exceed the modeled significance threshold. (v) Test that the modulus of both maxima and minima of the cross-correlation exceed the significance threshold. (vi) Test that the cross-correlation oscillation period is consistent with the average periods of its constituent waveforms. (vii) Determine the cross-correlation extremum closest to lag zero, A_n and lag τ_n. (viii) Amplitude A_n and lag τ_n classify the network connection between the two magnetometer stations as directed, undirected in-phase or undirected anti-phase.

Appendix B: Anti-Phase Network Response

The anti-phase response to the 2015 St. Patrick's Day storm is detailed in Figures B1 and B2. At onset the $\hat{n}$, $\hat{e}$ and $\hat{z}$ component network surrogate estimated SNR is significant ($\phi_{n,e,z} \approx 25$), for which we see a response in all sub-networks, similar to the in-phase network response. However, unlike the in-phase network response at onset $N_{n,e}/G_{n,e} > 1$. The surrogate estimated SNR remains high for the $\hat{n}$, $\hat{e}$ and $\hat{z}$ components ($\phi_{n,e,z} \approx 20$) from 6:20:00–08:15:00 UT. Approximately 30 min after the Pc2 power peak at 06:45:00 UT, we see an enhancement in connections between the northern and southern geomagnetic hemispheres relative to geomagnetic northern hemisphere connections, as $G_{n,e}/N_{n,e} > 1$ and corresponding to an increase in long-range connections as $L_{n,e}/S_{n,e} > 1$. From 08:15:00–10:15:00 UT all components have a high surrogate estimated SNR, with ($\phi_{n,e,z} \approx 20$) and short-range and northern hemisphere connections are enhanced for the $\hat{z}$ component as $N_z/G_z > 1$ and $S_z/L_z > 1$, when SME and Pc2 power peak, while SMR by MLT sector is close to minimum. Similarly to the in-phase networks, the number of sub-network connections reaches a peak at this time. An enhancement in northern hemisphere connections for the $\hat{z}$ component in-phase network is seen 35 min after the anti-phase response, with $N_z/G_z > 1$.

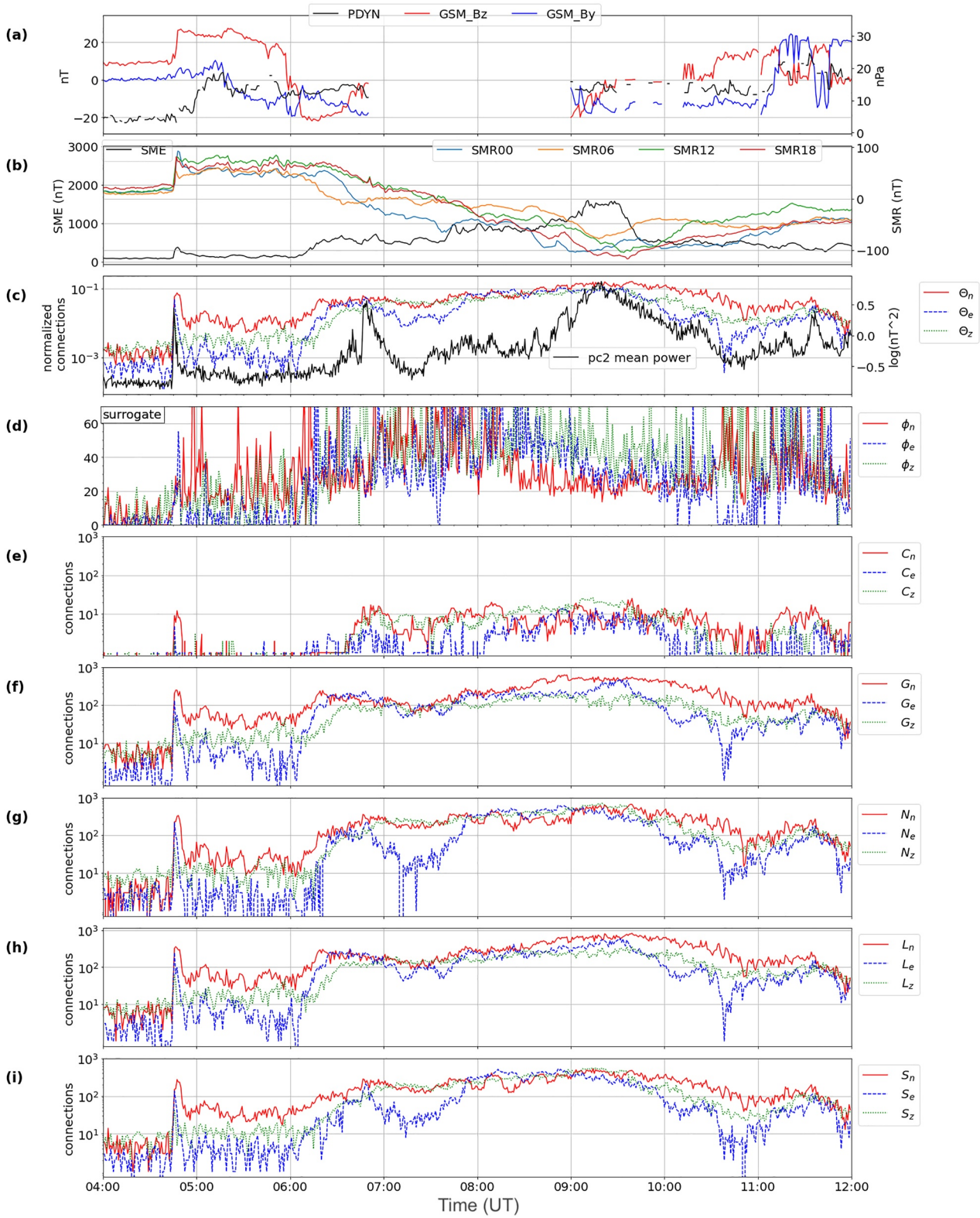

Figure B1. Event overview and anti-phase sub-networks. The panels (a)–(i) have the same format as Figure 1.

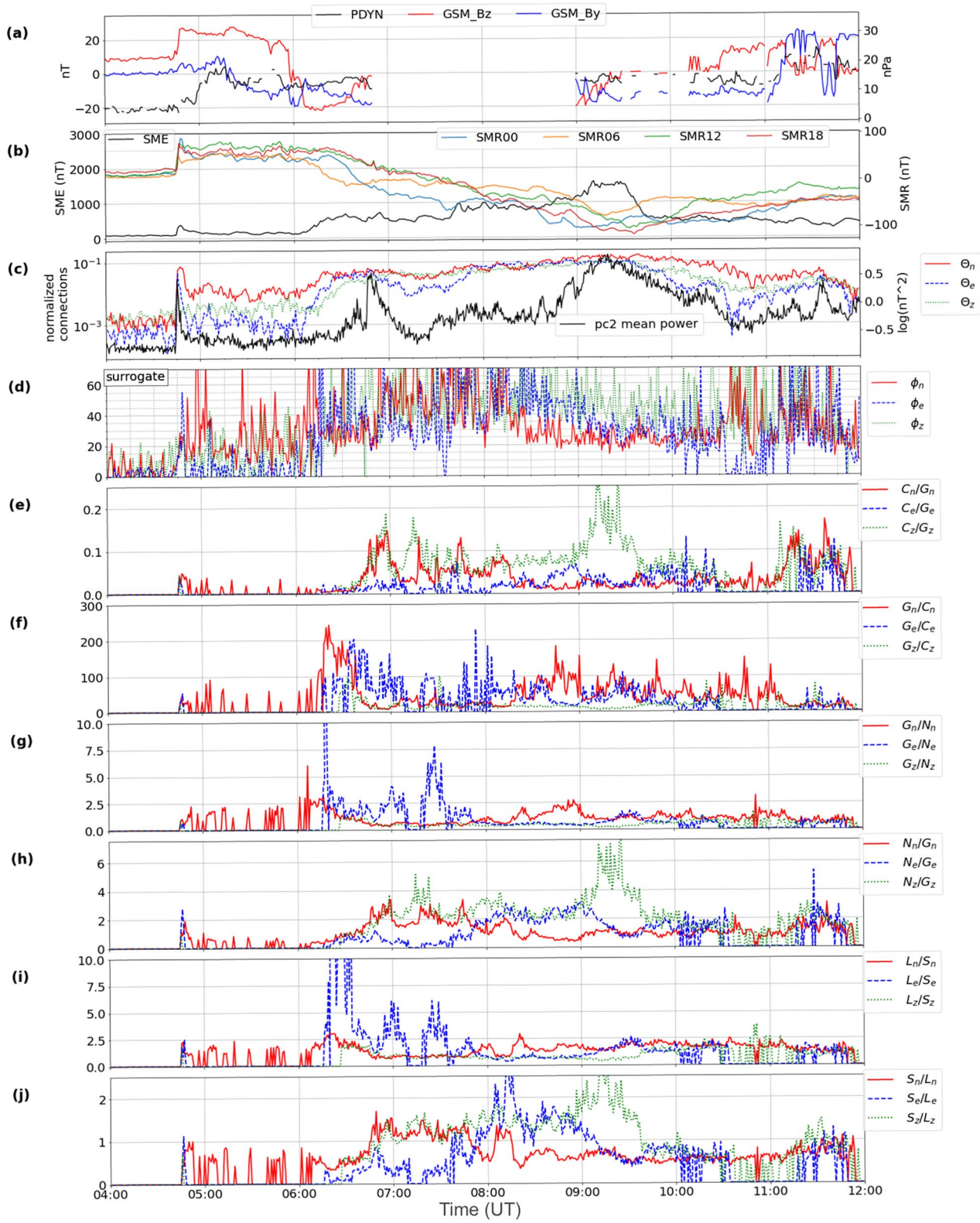

Figure B2. Event overview and anti-phase network parameters. The panels (a)–(j) have the same format as Figure 2.

Appendix C: In-Phase Network Snapshots

Here we show the in-phase network snapshots for the $\hat{e}$ and $\hat{z}$ component networks, where these networks behave differently from the $\hat{n}$ component network and have significant edges, Figures C1–C5. To compare component network snapshots we will use reference times $T1$–6 as seen in Figures 3–8. At time $T4$, the Pc2 power spikes and the $\hat{e}$ component network has a lower number of north-south (purple) connections compared to the $\hat{n}$ component network. However, at $T5$, the $\hat{e}$ and $\hat{z}$ component networks have more north-south connections than the $\hat{n}$ component network. The $\hat{e}$ component network at $T5$ has two distinct northern hemisphere clusters for connections limited to ΔMLT < 4 hr. Later at $T6$, the number of connections for all networks components is maximum and the degree distribution for $\hat{e}$ component sub-networks in Figure C4, panel (d) is broader with a lower average degree than the $\hat{n}$ component network. Compared to the global activity seen in the $\hat{n}$ component network snapshot at $T6$ the $\hat{z}$ component network shows that northern hemisphere (North American) connections dominate.

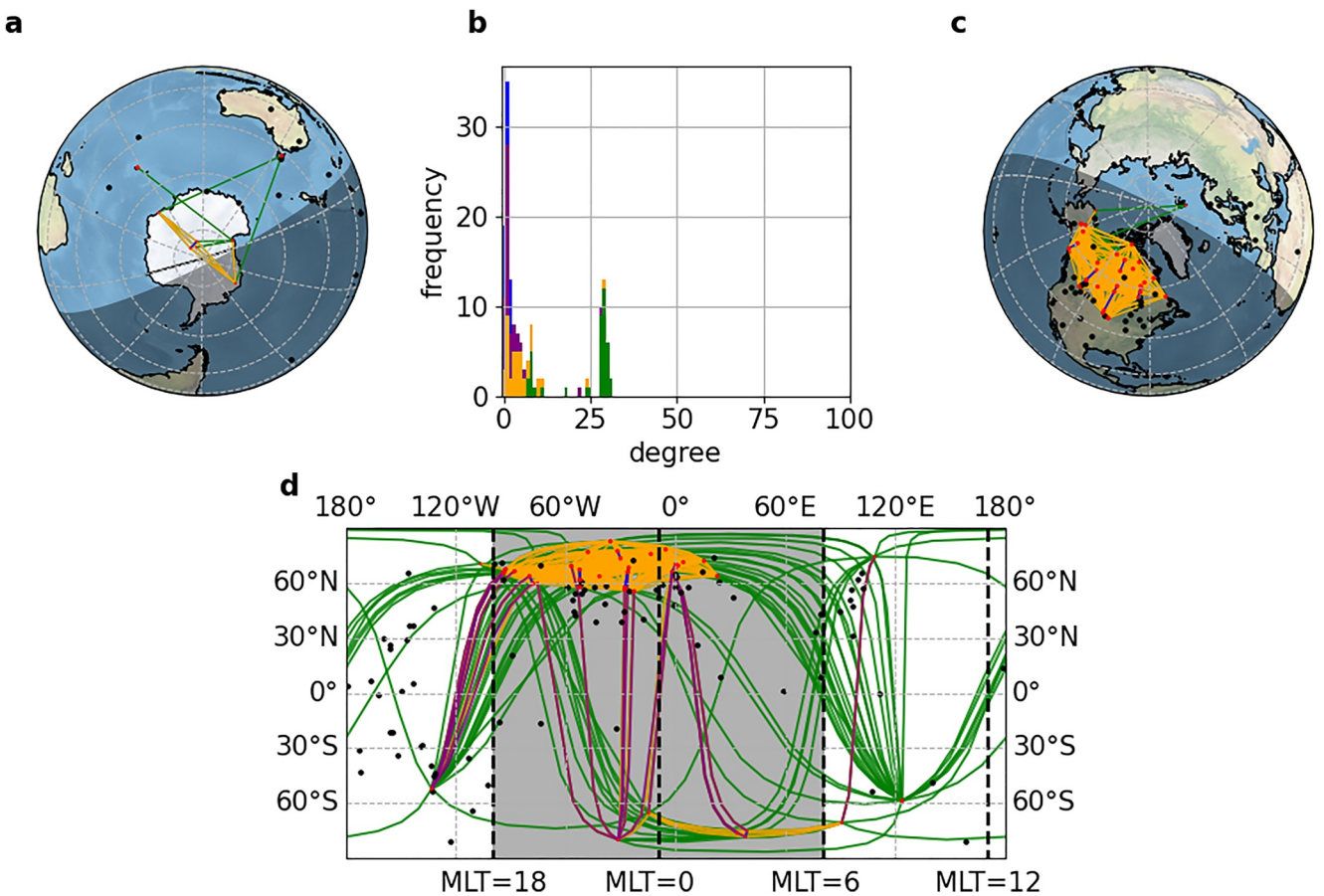

Figure C1. Network snapshot at $T4$ (06:45:50 UT) comprising 41 stations for the $\hat{e}$ component. The figure format is the same as Figure 3.

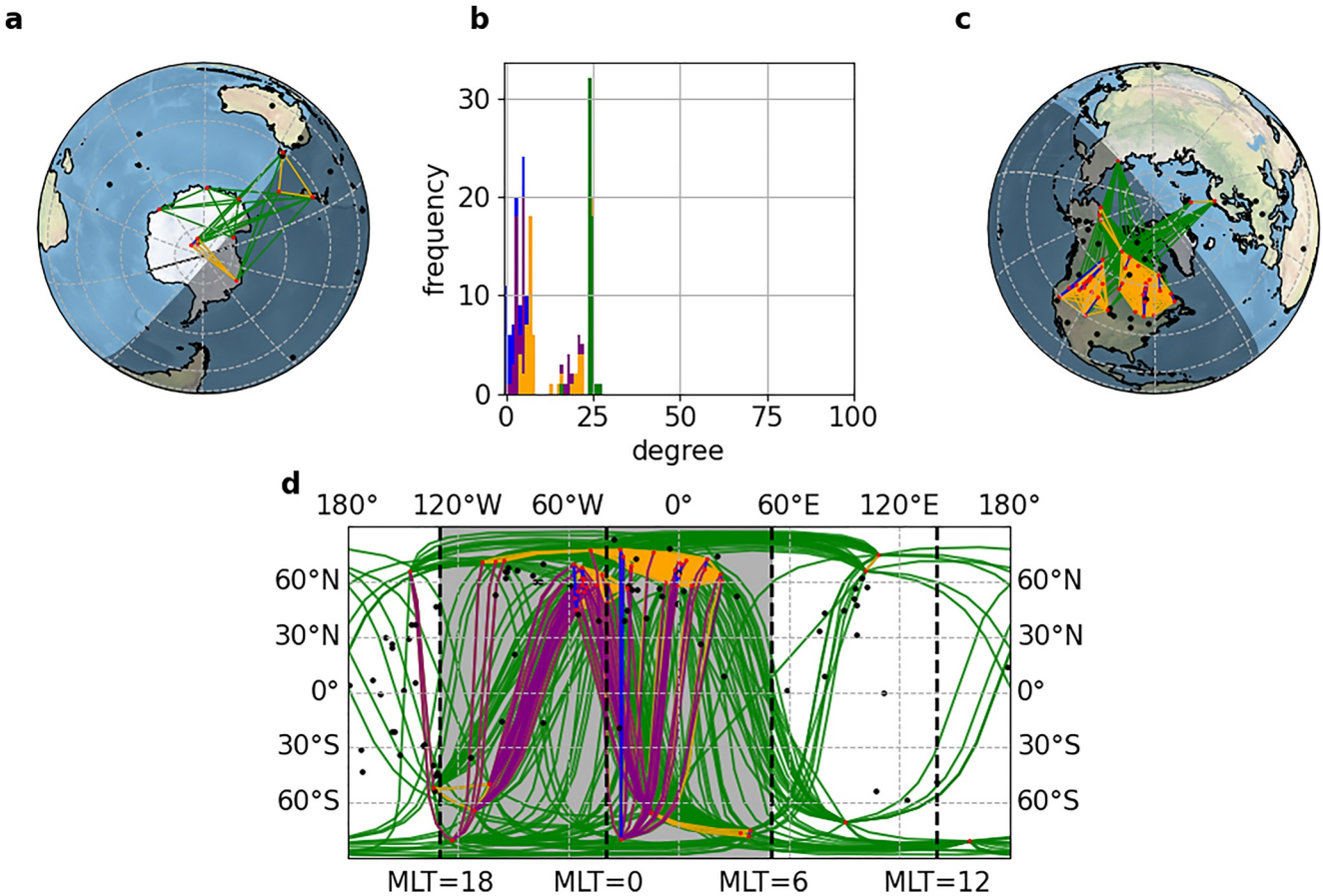

Figure C2. Network snapshot at *T*5 (08:18:00 UT) comprising 53 stations for the $\hat{e}$ component network. The figure format is the same as Figure 3.

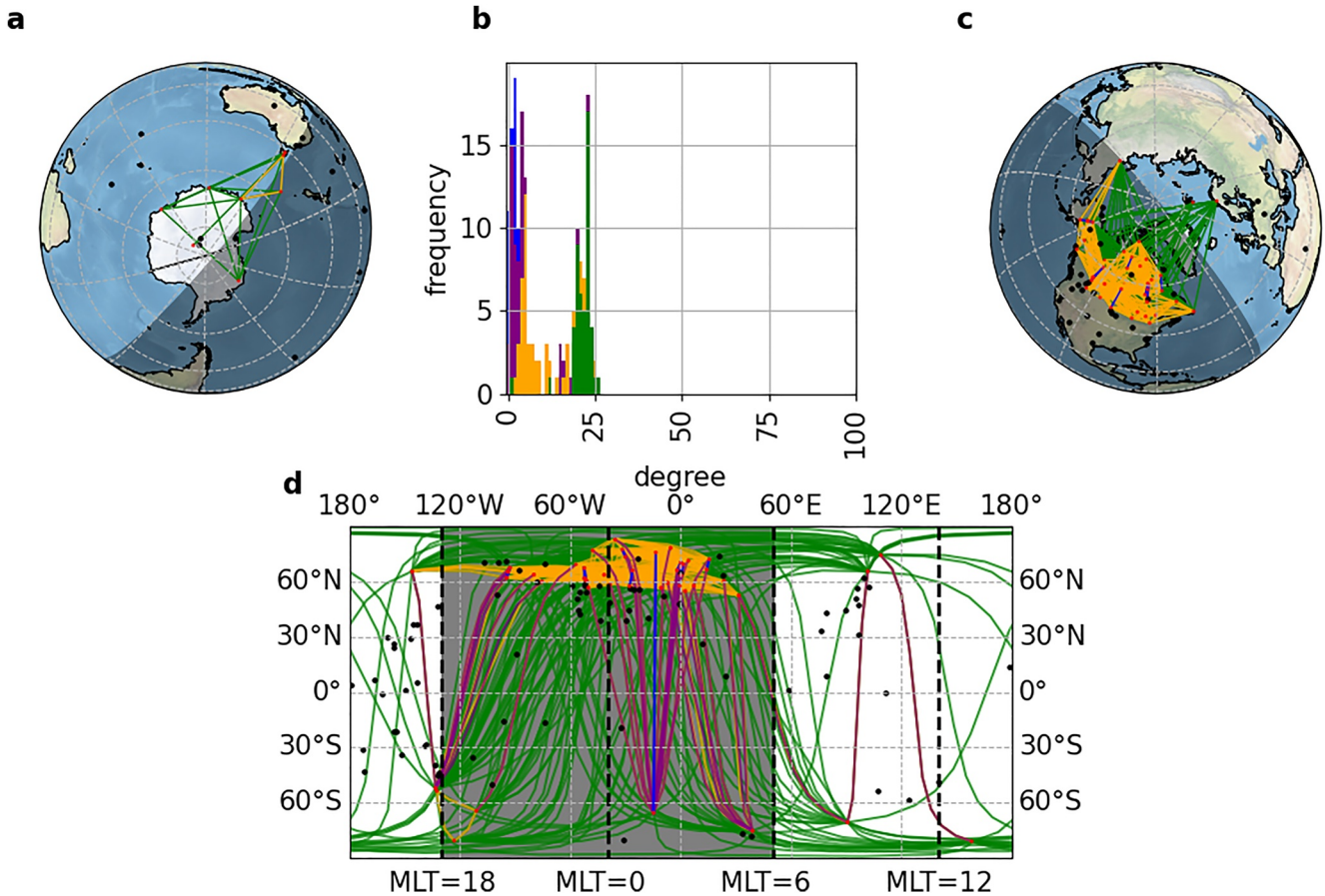

Figure C3. Network snapshot at *T*5 (08:18:50 UT) comprising 49 stations for the component network. The figure format is the same as Figure 3.

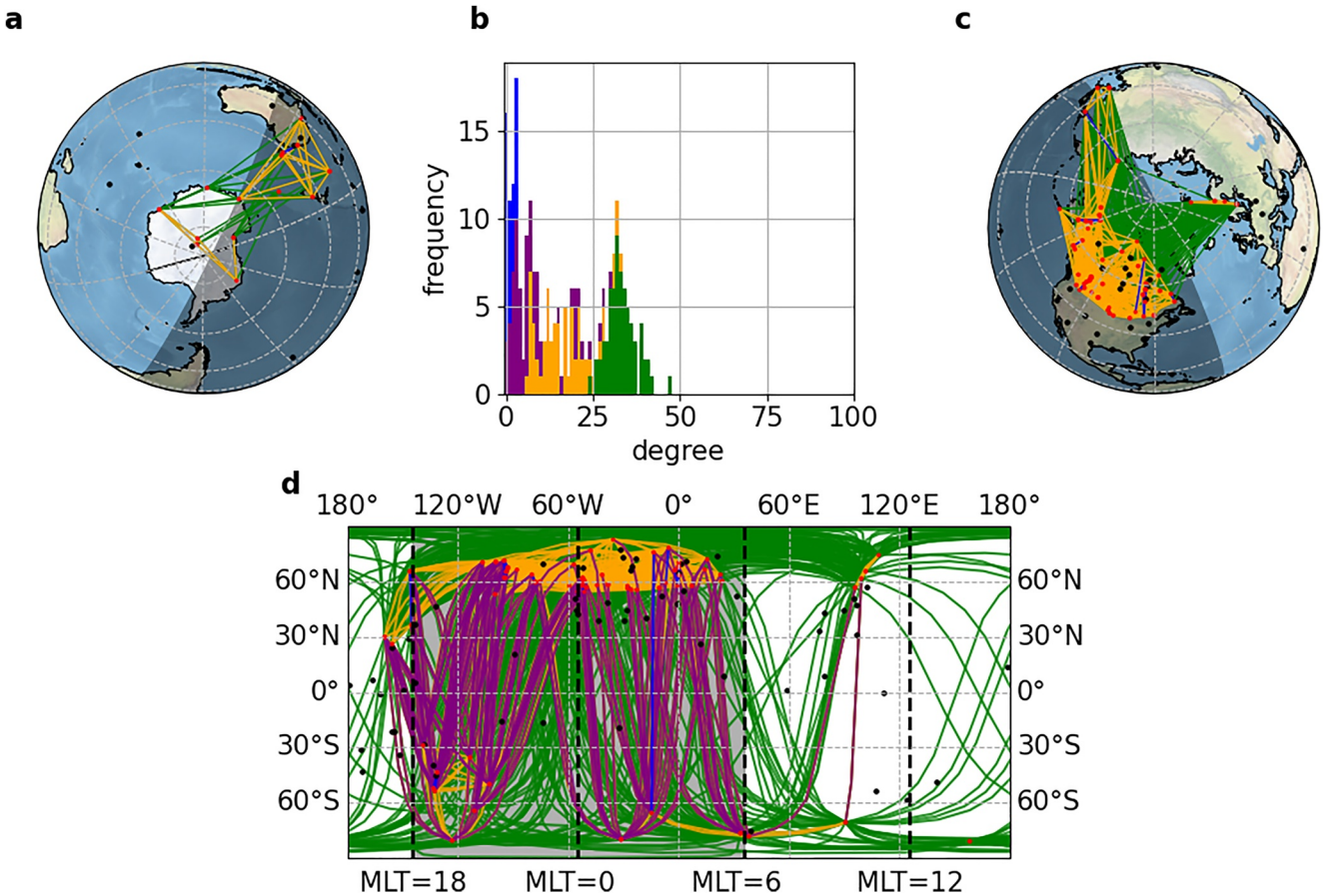

Figure C4. Network snapshot at *T*6 (09:15:00 UT) comprising 67 stations for the $\hat{e}$ component network. The figure format is the same as Figure 3.

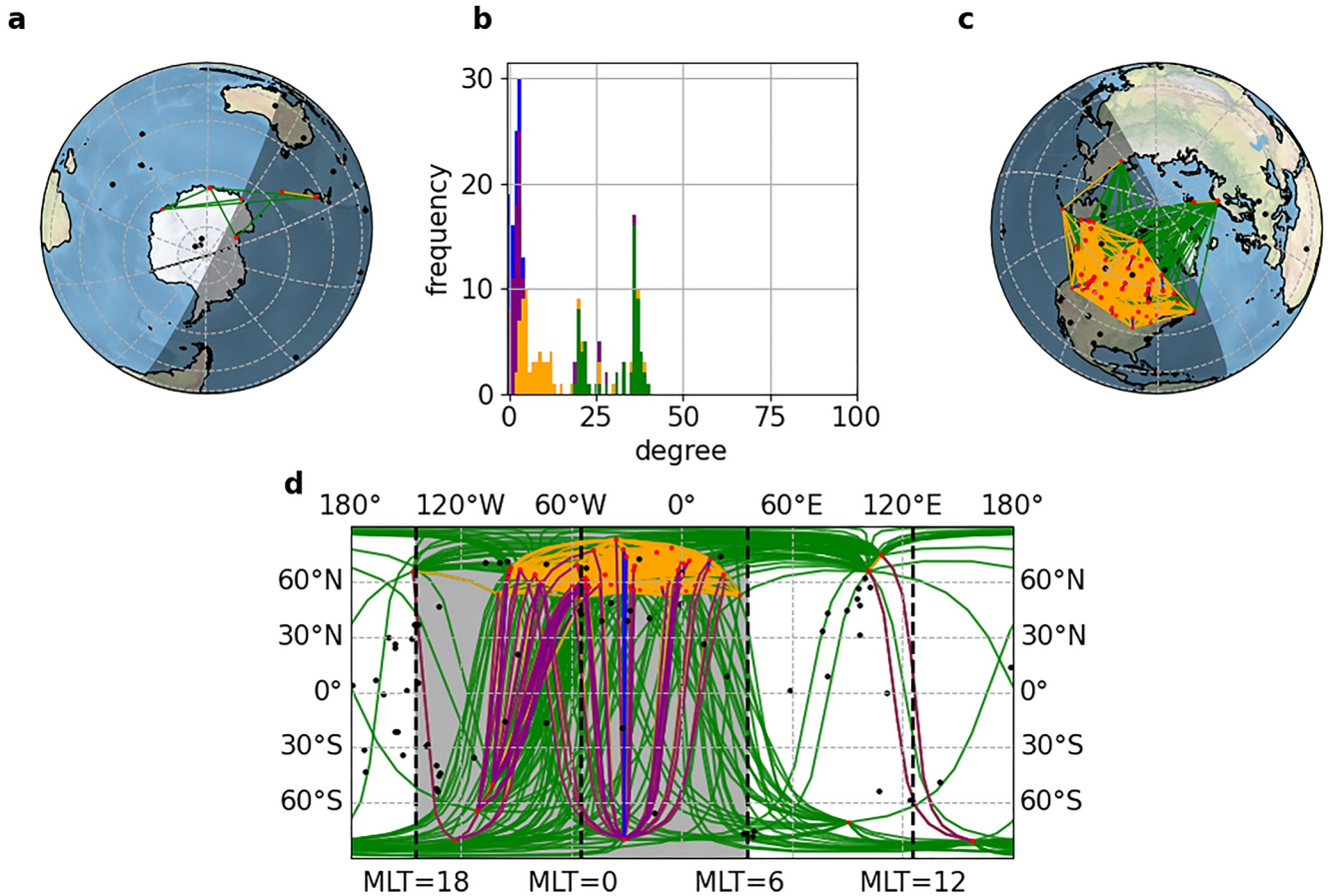

Figure C5. Network snapshot at *T*6 (09:15:00 UT) comprising 61 stations for the $\hat{z}$ component network. The figure format is the same as Figure 3.

Data Availability Statement

Data for 1 s resolution ground-based magnetometer time series is obtained from the SuperMAG (Gjerloev, 2012) and Intermagnet (Kerridge, 2001) collaborations (supermag.jhuapl.edu, intermagnet.org). Data downloaded on the 25th of October 2021. The ground-magnetometer station list is given in (SuperMAG, 2023). Figures were made with Python libraries Matplotlib version 3.5.1 (matplotlib.org) (Hunter, 2007) and Cartopy version 0.18.0 (scitools.org.uk/cartopy) (Met Office, 2010–2015). Software not publicly available, but available to researchers with appropriate credentials. We intend to make the code (with steps detailed in Figures A1 and A2) open source, however are currently in the prototype stage and intend to document and restructure the code for public reuse.

Acknowledgments
The results presented in this paper rely on data collected at magnetic observatories. We thank the national institutes that support them and Intermagnet and SuperMAG for promoting high standards of magnetic observatory practice. S.C. and S.C.C. acknowledge AFOSR grant FA8655-22-1-7056. This work has also benefited from discussions within the International Space Science Institute (ISSI), team 455, "Complex Systems Perspectives Pertaining to the Research of the Near-Earth Electromagnetic Environment." S.C.C. acknowledges STFC grant ST/T000252/1 and support from ISSI via the J. Geiss fellowship.

References

Abe, S., & Suzuki, N. (2006). Complex-network description of seismicity. *Nonlinear Processes in Geophysics*, *13*(2), 145–150. https://doi.org/10.5194/npg-13-145-2006

Arnoldy, R., Engebretson, M., Alford, J., Erlandson, R., & Anderson, B. (1996). Magnetic impulse events and associated Pc 1 bursts at dayside high latitudes. *Journal of Geophysical Research*, *101*(A4), 7793–7799. https://doi.org/10.1029/95ja03378

Astafyeva, E., Zakharenkova, I., & Förster, M. (2015). Ionospheric response to the 2015 St. Patrick's Day storm: A global multi-instrumental overview. *Journal of Geophysical Research: Space Physics*, *120*(10), 9023–9037. https://doi.org/10.1002/2015ja021629

Balasis, G., Daglis, I. A., Contoyiannis, Y., Potirakis, S. M., Papadimitriou, C., Melis, N. S., et al. (2018). Observation of intermittency-induced critical dynamics in geomagnetic field time series prior to the intense magnetic storms of March, June, and December 2015. *Journal of Geophysical Research: Space Physics*, *123*(6), 4594–4613. https://doi.org/10.1002/2017ja025131

Baumjohann, W., & Treumann, R. A. (2012). *Basic space plasma physics*. World Scientific Publishing Company.

Boccaletti, S., Latora, V., Moreno, Y., Chavez, M., & Hwang, D.-U. (2006). Complex networks: Structure and dynamics. *Physics Reports*, *424*(4–5), 175–308. https://doi.org/10.1016/j.physrep.2005.10.009

Butterworth, S. (1930). On the theory of filter amplifiers. *Wireless Engineer*, *7*(6), 536–541.

Castillo, E. (1998). Functional networks. *Neural Processing Letters*, *7*(3), 151–159. https://doi.org/10.1023/a:1009656525752

Chisham, G., & Orr, D. (1997). A statistical study of the local time asymmetry of Pc 5 ULF wave characteristics observed at midlatitudes by SAMNET. *Journal of Geophysical Research*, *102*(A11), 24339–24350. https://doi.org/10.1029/97ja01801

Clilverd, M. A., Rodger, C. J., Kamp, M. V. D., & Verronen, P. T. (2020). Electron precipitation from the outer radiation belt during the St. Patrick's Day storm 2015: Observations, modeling, and validation. *Journal of Geophysical Research: Space Physics*, *125*(2). https://doi.org/10.1029/2019JA027725

Dai, L., Takahashi, K., Wygant, J. R., Chen, L., Bonnell, J., Cattell, C. A., et al. (2013). Excitation of poloidal standing Alfvén waves through drift resonance wave-particle interaction. *Geophysical Research Letters*, *40*(16), 4127–4132. https://doi.org/10.1002/grl.50800

Del Corpo, A., Vellante, M., Heilig, B., Pietropaolo, E., Reda, J., & Lichtenberger, J. (2020). An empirical model for the dayside magnetospheric plasma mass density derived from EMMA magnetometer network observations. *Journal of Geophysical Research: Space Physics*, *125*(2), e2019JA027381. https://doi.org/10.1029/2019ja027381

Dods, J., Chapman, S., & Gjerloev, J. (2015). Network analysis of geomagnetic substorms using the SuperMAG database of ground-based magnetometer stations. *Journal of Geophysical Research: Space Physics*, *120*(9), 7774–7784. https://doi.org/10.1002/2015ja021456

Dods, J., Chapman, S., & Gjerloev, J. (2017). Characterizing the ionospheric current pattern response to southward and northward IMF turnings with dynamical SuperMAG correlation networks. *Journal of Geophysical Research: Space Physics*, *122*(2), 1883–1902. https://doi.org/10.1002/2016ja023686

Engebretson, M., Lessard, M., Bortnik, J., Green, J., Horne, R. B., Detrick, D., et al. (2008). Pc1–Pc2 waves and energetic particle precipitation during and after magnetic storms: Superposed epoch analysis and case studies. *Journal of Geophysical Research*, *113*(A1). https://doi.org/10.1029/2007ja012362

Gjerloev, J. (2012). The SuperMAG data processing technique. *Journal of Geophysical Research*, *117*(A9). https://doi.org/10.1029/2012ja017683

Gonzalez, W., Joselyn, J.-A., Kamide, Y., Kroehl, H. W., Rostoker, G., Tsurutani, B., & Vasyliunas, V. (1994). What is a geomagnetic storm? *Journal of Geophysical Research*, *99*(A4), 5771–5792. https://doi.org/10.1029/93ja02867

Hudson, M., Denton, R., Lessard, M., Miftakhova, E., & Anderson, R. (2004). A study of Pc-5 ULF oscillations. *Annales geophysicae*, *22*(1), 289–302. https://doi.org/10.5194/angeo-22-289-2004

Hughes, W. J. (1994). Magnetospheric ULF waves: A tutorial with a historical perspective. *Solar Wind Sources of Magnetospheric Ultra-Low-Frequency Waves*, *81*, 1–11.

Hunter, J. D. (2007). Matplotlib: A 2D graphics environment [Software]. Computing in Science & Engineering, *9*(03), 90–95. https://doi.org/10.1109/mcse.2007.55

Jacobs, J., Kato, Y., Matsushita, S., & Troitskaya, V. (1964). Classification of geomagnetic micropulsations. *Journal of Geophysical Research*, *69*(1), 180–181. https://doi.org/10.1029/jz069i001p00180

Jacobsen, K. S., & Andalsvik, Y. L. (2016). Overview of the 2015 St. Patrick's Day storm and its consequences for RTK and PPP positioning in Norway. *Journal of Space Weather and Space Climate*, *6*, A9. https://doi.org/10.1051/swsc/2016004

Katsavrias, C., Raptis, S., Daglis, I. A., Karlsson, T., Georgiou, M., & Balasis, G. (2021). On the generation of Pi2 pulsations due to plasma flow patterns around magnetosheath jets. *Geophysical Research Letters*, *48*(15), e2021GL093611. https://doi.org/10.1029/2021gl093611

Kerridge, D. (2001). INTERMAGNET: Worldwide near-real-time geomagnetic observatory data. In *Proceedings of the workshop on space weather* (Vol. 34). ESTEC.

Kitamura, T.-i., Saka, O., Shimoizumi, M., Tachihara, H., Oguti, T., Araki, T., et al. (1988). Global mode of Pi2 waves in the equatorial region difference of Pi2 mode between high and equatorial latitudes. *Journal of Geomagnetism and Geoelectricity*, *40*(5), 621–634. https://doi.org/10.5636/jgg.40.621

Kozma, B., & Barrat, A. (2008). Consensus formation on adaptive networks. *Physical Review E*, *77*(1), 016102. https://doi.org/10.1103/physreve.77.016102

Kozyra, J., Jordanova, V., Home, R., & Thorne, R. (1997). Modeling of the contribution of electromagnetic ion cyclotron (EMIC) waves to storm-time ring current erosion. *Washington DC American Geophysical Union Geophysical Monograph Series*, *98*, 187–202.

Lancaster, G., Iatsenko, D., Pidde, A., Ticcinelli, V., & Stefanovska, A. (2018). Surrogate data for hypothesis testing of physical systems. *Physics Reports*, *748*, 1–60. https://doi.org/10.1016/j.physrep.2018.06.001

Li, Z., Hudson, M., Patel, M., Wiltberger, M., Boyd, A., & Turner, D. (2017). ULF wave analysis and radial diffusion calculation using a global MHD model for the 17 March 2013 and 2015 storms. *Journal of Geophysical Research: Space Physics*, *122*(7), 7353–7363. https://doi.org/10.1002/2016ja023846

Liu, Y., Fraser, B., & Menk, F. (2012). Pc2 EMIC waves generated high off the equator in the dayside outer magnetosphere. *Geophysical Research Letters*, *39*(17). https://doi.org/10.1029/2012gl053082

Mahrous, A. M., Ibrahim, M., Berdermann, J., & Salah, H. M. (2018). Ionospheric scintillations detected by SCINDA-Helwan station during St. Patrick's Day geomagnetic storm. *NRIAG Journal of Astronomy and Geophysics*, *7*(2), 214–219. https://doi.org/10.1016/J.NRJAG.2018.05.007

Maurya, A. K., Venkatesham, K., Kumar, S., Singh, R., Tiwari, P., & Singh, A. K. (2018). Effects of St. Patrick's Day geomagnetic storm of March 2015 and of June 2015 on low-equatorial D region ionosphere. *Journal of Geophysical Research: Space Physics*, *123*(8), 6836–6850. https://doi.org/10.1029/2018JA025536

McGranaghan, R. M., Mannucci, A. J., Verkhoglyadova, O., & Malik, N. (2017). Finding multiscale connectivity in our geospace observational system: Network analysis of total electron content. *Journal of Geophysical Research: Space Physics*, *122*(7), 7683–7697. https://doi.org/10.1002/2017ja024202

McPherron, R., Russell, C., & Coleman, P. (1972). Fluctuating magnetic fields in the magnetosphere. *Space Science Reviews*, *13*(3), 411–454. https://doi.org/10.1007/bf00173072

Menk, F. W. (2011). Magnetospheric ULF waves: A review. In *The dynamic magnetosphere* (pp. 223–256). Springer.

Met Office. (2010–2015). Cartopy: A cartographic python library with a matplotlib interface [Software]. Retrieved from https://scitools.org.uk/cartopy. Cartopy

Moen, J., Hosokawa, K., Gulbrandsen, N., & Clausen, L. B. N. (2015). On the symmetry of ionospheric polar cap patch exits around magnetic midnight. *Journal of Geophysical Research: Space Physics*, *120*(9), 7785–7797. https://doi.org/10.1002/2014ja020914

Murphy, K. R., Mann, I. R., & Ozeke, L. G. (2014). A ULF wave driver of ring current energization. *Geophysical Research Letters*, *41*(19), 6595–6602. https://doi.org/10.1002/2014gl061253

Newell, P., & Gjerloev, J. (2012). SuperMAG-based partial ring current indices. *Journal of Geophysical Research*, *117*(A5). https://doi.org/10.1029/2012ja017586

Newman, M. (2018). *Networks*. Oxford University Press.

Nosé, M., Iyemori, T., Wang, L., Hitchman, A., Matzka, J., Feller, M., et al. (2012). Wp index: A new substorm index derived from high-resolution geomagnetic field data at low latitude. *Space Weather*, *10*(8), 1–12. https://doi.org/10.1029/2012sw000785

Orr, L., Chapman, S., & Gjerloev, J. (2019). Directed network of substorms using SuperMAG ground-based magnetometer data. *Geophysical Research Letters*, *46*(12), 6268–6278. https://doi.org/10.1029/2019gl082824

Orr, L., Chapman, S. C., & Beggan, C. D. (2021). Wavelet and network analysis of magnetic field variation and geomagnetically induced currents during large storms. *Space Weather*, *19*(9), e2021SW002772. https://doi.org/10.1029/2021sw002772

Orr, L., Chapman, S. C., Gjerloev, J. W., & Guo, W. (2021). Network community structure of substorms using SuperMAG magnetometers. *Nature Communications*, *12*(1), 1–10. https://doi.org/10.1038/s41467-021-22112-4

Papitashvili, N., Bilitza, D., & King, J. (2014). OMNI: A description of near-earth solar wind environment. In *40th COSPAR scientific assembly* (Vol. 40, no. C0–1)

Pastén, D., Czechowski, Z., & Toledo, B. (2018). Time series analysis in earthquake complex networks. *Chaos: An Interdisciplinary Journal of Nonlinear Science*, *28*(8), 083128. https://doi.org/10.1063/1.5023923

Pearson, K. (1896). VII. Mathematical contributions to the theory of evolution.—III. Regression, heredity, and panmixia. *Philosophical Transactions of the Royal Society of London—Series A: Containing Papers of a Mathematical or Physical Character*, *187*, 253–318.

Poppe, B. B. (2000). New scales help public, technicians understand space weather. *Eos, Transactions American Geophysical Union*, *81*(29), 322–328. https://doi.org/10.1029/00eo00247

Pulkkinen, T. (2007). Space weather: Terrestrial perspective. *Living Reviews in Solar Physics*, *4*(1), 1. https://doi.org/10.12942/lrsp-2007-1

Rasinkangas, R., Mursula, K., Kremser, G., Singer, H., Fraser, B., Korth, A., & Hughes, W. (1994). Simultaneous occurrence of Pc 5 and Pc 1 pulsations in the dawnside magnetosphere: CRRES observations. *Geophysical Monograph-American Geophysical Union*, *81*, 417.

Schreiber, T., & Schmitz, A. (2000). Surrogate time series. *Physica D: Nonlinear Phenomena*, *142*(3–4), 346–382. https://doi.org/10.1016/s0167-2789(00)00043-9

Schwenn, R. (2006). Space weather: The solar perspective. *Living Reviews in Solar Physics*, *3*(1), 2. https://doi.org/10.12942/lrsp-2006-2

Southwood, D., & Hughes, W. (1983). Theory of hydromagnetic waves in the magnetosphere. *Space Science Reviews*, *35*(4), 301–366. https://doi.org/10.1007/bf00169231

Strogatz, S. H. (2001). Exploring complex networks. *Nature*, *410*(6825), 268–276. https://doi.org/10.1038/35065725

SuperMAG. (2023). Ground-magnetometer station list [Dataset]. SuperMAG. Retrieved from https://supermag.jhuapl.edu/mag/?fidelity=high&tab=stationinfo&start=2001-01-01T00%3A00%3A00.000Z&interval=00%3A23%3A59

Todd, H., Cowley, S., Lockwood, M., Willis, D., & Lühr, H. (1988). Response time of the high-latitude dayside ionosphere to sudden changes in the north-south component of the IMF. *Planetary and Space Science*, *36*(12), 1415–1428. https://doi.org/10.1016/0032-0633(88)90008-6

Wu, C. C., Liou, K., Lepping, R. P., Hutting, L., Plunkett, S., Howard, R. A., & Socker, D. (2016). The first super geomagnetic storm of solar cycle 24: "the St. Patrick's Day event (17 march 2015)" global data systems for the study of solar-terrestrial variability. *Earth Planets and Space*, *68*(1), 1–12. https://doi.org/10.1186/S40623-016-0525-Y

Yumoto, K. (1988). External and internal sources of low-frequency MHD waves in the magnetosphere-a review. *Journal of Geomagnetism and Geoelectricity*, *40*(3), 293–311. https://doi.org/10.5636/jgg.40.293

Yumoto, K. (2006). MAGDAS project and its application for space weather. In *Proceedings of the ILWS workshop* (p. 399).

Ziesolleck, C., & McDiarmid, D. (1994). Auroral latitude Pc 5 field line resonances: Quantized frequencies, spatial characteristics, and diurnal variation. *Journal of Geophysical Research*, *99*(A4), 5817–5830. https://doi.org/10.1029/93ja02903